PHOTONICS Research

Micro- and nano-fiber probes for optical sensing, imaging, and stimulation in biomedical applications

Xia Yu,[1,*] Shuyan Zhang,[2] Malini Olivo,[2] and Nanxi Li[3]

[1]School of Instrumentation and Optoelectronic Engineering, Beihang University, Beijing 100083, China
[2]Singapore Bioimaging Consortium, Agency for Science, Technology, and Research (A*STAR), Singapore 138667, Singapore
[3]Institute of Microelectronics, Agency for Science, Technology, and Research (A*STAR), Singapore 138634, Singapore
*Corresponding author: xiayu@BUAA.edu.cn

The flexibile nature of optical fiber enables it to offer remote-access capabilities, which could be used in many biomedical applications. This review focuses on different micro- and nano-structured fiber probes for applications in biosensing, imaging, and stimulations. The modifications to fiber could extend design freedom from waveguide optimization to functional material integration. Fiber probes with optimized waveguide structures or integrated functional materials could achieve enhanced optical mode interaction with biosamples, and hence obtain ultra-sensitive biosensors with a remarkably low limit of detection. Furthermore, bioimaging with a high spatial resolution can be obtained by engineering dispersion and nonlinearity of light propagation in the fiber core or designing a metal-coated tapered fiber tip with a sub-wavelength aperture. Flat metasurfaces can be assembled on a fiber tip to achieve a large depth of focus and remove aberrations. Fiber is also a compact solution to realize the precise delivery of light for *in vivo* applications, such as deep brain stimulation. The optical beam size, shape, and direction could be steered by the probe parameters. Micro- and nano-technologies integrated with fiber contribute to various approaches to further improve detection limit, sensitivity, optical resolution, imaging depth, and stimulation precision. © 2020 Chinese Laser Press

https://doi.org/10.1364/PRJ.387076

1. INTRODUCTION

Optical fiber is a type of attractive waveguide offering advantages including low propagation loss, high flexibility, lightweight, and electromagnetic interference immunity. They also have special optical properties, which make them a suitable platform for lasers, amplifiers, and nonlinear optical generation [1–8]. In addition, optical fibers are also compatible with biological substances since they are mostly made of silica or polymer materials [9,10].

There are several typical groups of biomedical applications that take advantage of the flexibility and compactness of optical fibers to achieve remote delivery of light, such as optical biosensing, optical imaging, and optical stimulation. Aiming for single-molecule detection, optical biosensing technologies challenge the limit of detection (LOD). Making the fiber outer diameter down to a few micrometers or even submicrometer dimensions enhances the light–matter interaction [11,12]. The selection of new materials at the interface between fiber and bioanalyte helps to improve sensing performance [13,14]. The water dispersibility and biomolecule affinity are crucial factors while maintaining high-sensitivity performance.

Visualization of bio-organisms requires improved imaging resolution, especially for the *in vivo* modality. Fiber-based imaging with a high spatial resolution is controlled by the light field in the fiber core which is closely related to the microfiber or nanofiber probe parameters. The challenges remain in removing various aberrations, achieving a larger field of view and deeper imaging depth when designing the fiber-based catheter for 3D imaging [15]. Moreover, engineering the optical waveguide dispersion, nonlinearity, and polarization-maintaining properties are other important perspectives when moving to ultrafast laser-based nonlinear optical imaging [16].

Optical stimulation is a process of targeting a light beam to a specific nucleus. The combination of optical stimulation with genetic engineering paves the way for optogenetics [17]. Bioengineering of light-sensitive ion channels from the bacteria has made it possible to utilize light to modulate neuronal activity artificially. The precise manipulation of the beam is essential for selective control of the activity of neurons. Fiber optics probe becomes a preferred choice of implantable optrode [18] to regulate behavior and physiological functions.

References [19–22] review fiber-based biosensors from the perspectives including grating structures, plasmonic resonance

schemes, and lab-on-fiber technology. References [23–25] review fiber-based bioimaging techniques such as fluorescent imaging systems. Based on these reviews, we aim to provide a different perspective focusing on advanced fiber probe designs, i.e., microstructured and nanostructured fibers, for biophotonics applications. The modifications on the fiber or in the fiber could extend the device design freedom from waveguide modification to functional material integration. Also, this review covers special fiber probes for optical stimulation which is an emerging field in the biomedical community.

2. FIBER PROBES FOR BIOSENSING

Fiber-based biosensors have gained a lot of interest from research and development contributed by the advantages of fiber waveguides mentioned above. In this section, a summary of the optical fiber-based biosensors is presented, which is categorized based on their working principles. The focus is how the probe designs can help to improve the sensing performance. Driven by the motivation of high sensitivity and low detection limit of the biological samples, we will start with a surface resonance-based biosensor, followed by an interference-based biosensor, considering both are able to enhance the sensing signal. For each type of the above two fiber-based biosensors, the sensing principle is included, and the selected recent works within the past 5 years are summarized in a table. Typical schematics from each category of the fiber-based sensor are selected, with sensing performance results presented as well.

A. Resonance-Based Optical Fiber Sensors

1. Plasmon Resonance-Based Fiber Sensors

The traditional approach to excite the surface plasmon resonance (SPR) on a metallic–dielectric interface is by using a prism to inject light onto the interface. In comparison, the optical fiber-based plasmonic biosensors utilize the microscale/nanoscale fiber structure to excite the SPR, contributed by the compactness of the optical fiber. The optical fiber was originally designed to guide waves through total internal reflection at the interface between the core and the cladding. To make the core-guided light interact with the metal coatings or nanoparticles (NPs) attached to the fiber, modifications need to be done on the optical fiber structure, as summarized in the following three approaches. The first approach is to remove the cladding of the fiber via chemical etching or side-polishing to form D-shaped fibers, including standard step-index fibers [26–33] and microstructure fibers [34]. The refractometric sensitivity can reach 22,779 nm/refractive index unit (RIU) [32]. The schematic of the experiment is shown in Fig. 1(a) left panel, with the fiber cross section illustrated in the inset. The experimental result is shown in Fig. 1(a) right panel, illustrating the normalized transmission spectra under different glucose solution concentrations. The redshift of the SPR resonant wavelength can be observed as glucose concentration increases. After doing the fitting of the resonance wavelength versus glucose solution mass concentration, an averaged sensitivity of 24.50 nm/wt.%, which corresponds to an RI sensitivity of 17,560 nm/RIU, can be obtained. Figure 1(b) inset shows the cross section of a typical D-shaped microstructure fiber for an SPR-based sensor. The polished fiber is used for the dem-

onstration of plasmonic-enhanced fluorescence emission from rhodamine (Rh) B. The fluorescence emission spectra of Rh B are shown in Fig. 1(b). The distinction between the excitation and emission is achieved through the energy coupling from the surface plasmon wave of thin gold film to Rh B molecules. The second approach is to make tapered fibers with a thinner core so that the evanescent wave can interact with the metal coating on the tapered facet [35–38]. Its refractometric sensitivity can reach 20,300 nm/RIU [37]. In addition to that, electron-rich two-dimensional material can also be coated on the tapered fiber to provide strong SPR at a visible wavelength for biosensing with an ultralow LOD of 1 pg/mL [39]. The third approach is to coat the metal on the inner wall of the air holes containing analyte solutions in a microstructured fiber. Different fiber structure designs have been proposed for this approach [40–43]. A typical cross section of the microstructured fiber is illustrated in Fig. 1(c).

In comparison with the SPR, which is a lossy propagation wave along the metal surface [20], the localized surface plasmon resonance (LSPR) is an enhanced physical phenomenon. It is the localized electromagnetic wave trapped within metallic NPs with a sub-wavelength scale. A typical schematic of an LSPR-based fiber biosensor is shown in Fig. 1(d) left panel, making use of gold nanorods coated on the fiber core. The advantage of using NPs is contributed by the increase of the surface area and roughness [20]. Therefore, the biosensor based on the LSPR can achieve low analytes concentration detection [44–49]. Figure 1(d) right panel shows the sensing result of ochratoxin A (OTA) with concentrations varying from 0 μM to 1 μM (1 M = 1 mol/L). A redshift of the LSPR peak in spectra can be observed as the OTA concentration increases. An LOD of 12 pM was obtained by taking 3 times of the standard deviation of the measured signal with blank samples. Furthermore, in a recent work, a low LOD of 5 aM has been demonstrated using the LSPR from Au NPs coated on a tapered fiber [50], with the fiber schematic and measurement result shown in Fig. 1(e) left and right panels, respectively. The black curve in the measurement result illustrates the stabilized LSPR peak due to the Au NPs on the microfiber surface. The coated microfiber is immersed in cholesterol solutions with concentrations from 5 aM to 0.5 μM, and the transmissions under different concentrations have been plotted. The distinguishable deepening of the attenuation band can be observed. Low LOD of 5 aM is contributed by the efficient interaction between β-cyclodextrin-capped Au NPs and the cholesterol molecules.

Another type of resonance-based fiber sensor is making use of the lossy mode resonance (LMR) created by depositing thin film as lossy cladding for the waveguide [51]. As the original optical mode from fiber interacts with the deposited thin film, it will experience a transition to be guided within the film [22]. Such transition creates wavelength-dependent loss in the optical fiber. Figure 1(f) left panel shows the schematic of a recently reported LMR-based fiber biosensor. By using the LMR on a SnO_2-coated D-shaped fiber, a record low LOD of 1 fM and high sensitivity are achieved [52]. The experimental result is shown in Fig. 1(f) right panel. It illustrates the LMR wavelength with respect to different antigen concentrations
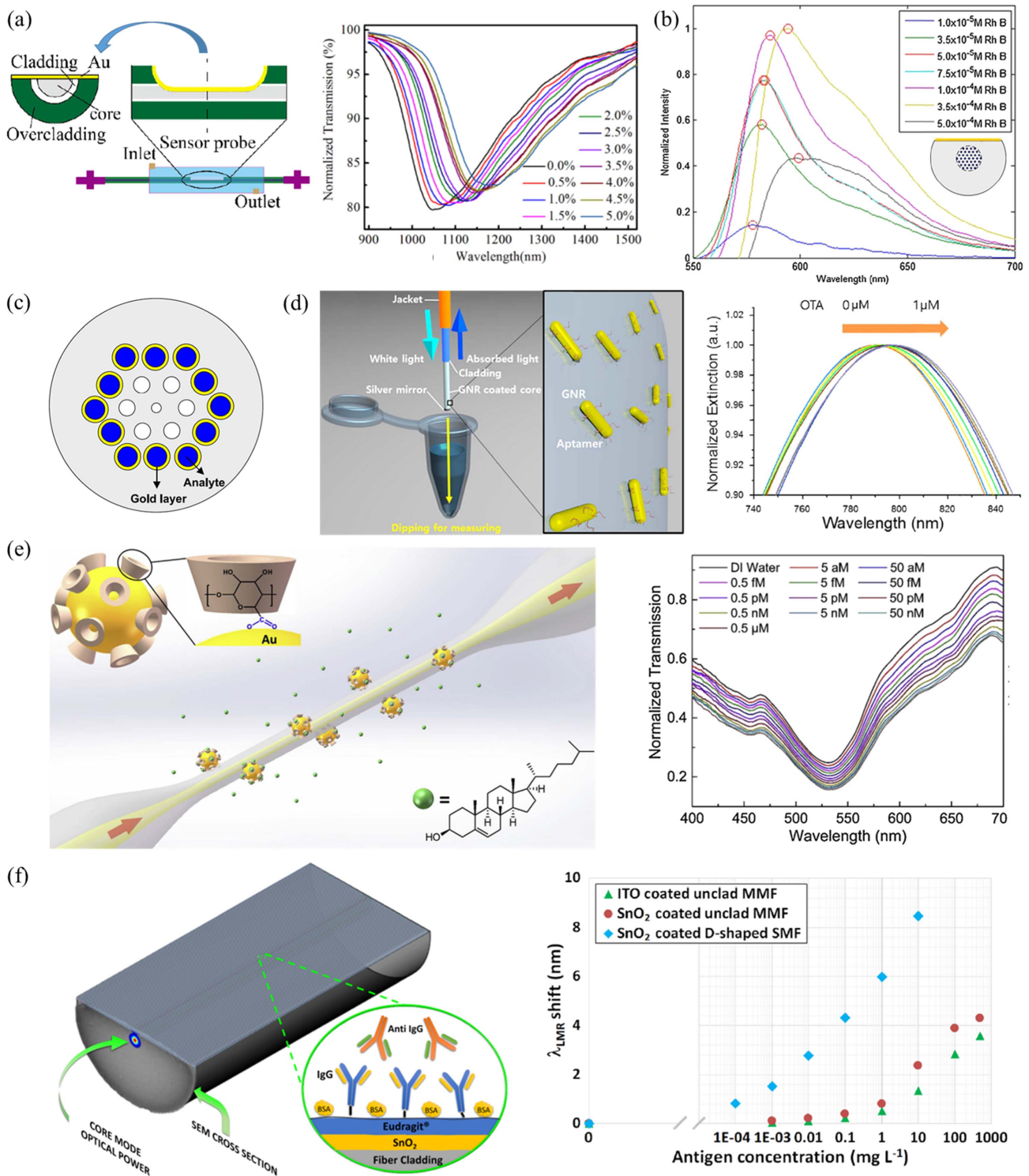
Fig. 1. Plasmon resonance-based fiber sensors. (a) Left: schematic of the fiber biosensor based on SPR with cladding partially polished for mode overlap with the metal layer. Right: normalized transmission spectra of the SPR-based sensor under different concentrations of glucose solution. (Adapted with permission from [32]. Copyright Optical Society of America.) (b) Fluorescence emission spectrum of Rh B under different concentrations in side-polished microstructured fiber with gold coating. Inset: cross section of D-shaped microstructured fiber with gold coated on top surface. (Adapted with permission from [34]. Copyright 2011 Elsevier.) (c) Microstructured fiber with Au coated on the inner wall of the air hole filled with analyte solution. (Adapted with permission from [40]. Copyright IOP Publishing.) (d) Left: schematic of fiber biosensor based on LSPR with Au nanorods coated on the fiber core. Right: normalized excitation spectrum showing LSPR redshift as OTA concentration increases. (Adapted with permission from [44]. Copyright 2018 Elsevier.) (e) Left: LSPR with Au NPs coated on tapered fiber, demonstrating an ultralow LOD of 5 aM. Right: sensing result showing the variation of transmission spectrum as the cholesterol concentration increases. (Reprinted with permission from [50]. Copyright 2019 Elsevier.) (f) Left: LMR with either SnO_2 or indium tin oxide (ITO) coated on D-shaped single-mode fiber (SMF) or unclad multimode fiber (MMF). Right: LMR shift with respect to antigen concentration for three kinds of LMR sensors. (Adapted with permission from [52]. Copyright 2018 American Chemical Society.)

Table 1. Summary of Recent Plasmon-Resonance-Based Optical Fiber Biosensors

Sensing Mechanism	Functional Material	Wavelength	Analyte	Sensitivity	LOD[a]	Ref.
SPR (on D-shaped fiber)	Au	750–1200 nm	Glucose	0.46 nm/mM	–	[32] (2018)
SPR (on unclad fiber)	Graphene oxide and Ag	500–650 nm	Immunoglobulin G (IgG)	0.4985 nm/(μg/mL)	0.04 μg/mL	[53] (2018)
LSPR (on tapered fiber)	Au NPs	400–700 nm	Cholesterol	–	5 aM	[50] (2019)
LSPR (on tapered fiber)	Au NPs	∼607 nm	Cholesterol	0.125%/mM (resonance intensity change/ concentration change)	53.1 nM	[49] (2019)
LSPR (on unclad fiber)	Au nanorods	∼790 nm	Ochratoxin A	601.05 nm/RIU	12 pM	[44] (2018)
LMR (on unclad or D-shaped fiber)	ITO or SnO$_2$	∼570 nm (ITO) ∼1460 nm (SnO$_2$)	IgG	–	23 pM (ITO on MMF) 1 fM (SnO$_2$ on D-shaped SMF)	[52] (2018)
LMR (on D-shaped fiber)	ITO	1380–1480 nm	C-reactive protein	10–169 nm/(mg/L)	0.0625 mg/L	[54] (2017)

[a]Limit of detection (LOD): the unit of molarity (M), concentration (mg/L or ppm) can be converted using the equation: molarity = concentration/molar mass.

for three kinds of sensors: indium tin oxide (ITO)- and SnO$_2$-coated unclad multimode fiber (MMF) biosensors, and SnO$_2$-coated D-shaped single-mode fiber (SMF) biosensors. The LOD of 1 fM is obtained using the D-shaped SMF biosensor with repeatability and reproducibility. The record low LOD and high sensitivity are contributed by the enhanced light–matter interaction within the fiber sensor structure. The selected recent works within the past 5 years on plasmon resonance-based fiber sensors, including SPR, LSPR, and LMR, are summarized in Table 1.

2. Surface-Enhanced Raman-Scattering-Based Fiber Biosensor

Raman spectroscopy has been widely applied in the detection of bioanalyte since it can identify the spectral characteristics or fingerprint of the biomolecules, while the detection is limited by the intrinsic low efficiency of the Raman effect. To enhance the Raman signal, the surface-enhanced Raman scattering (SERS) technique is commonly used [55–64]. The additional coating on the surface increases the roughness and enhances the optical mode through the localization of the signal generated from the Raman scattering. For most of the SERS-based fiber sensors, the backscattered signal, which is the combination of Raman gain and the metallic loss, is collected from the same side of the launching probe signal [65–72], as shown in Figs. 2(a) and 2(b); while a few are based on the detected signal from the forward propagating direction [73,74]. Both backward and forward signal detection approaches have been included in Table 2, which presents the selected recent works on SERS-based fiber sensors within the past 5 years.

There are two common methodologies to implement SERS functionality on optical fiber [21]: (1) to coat the metallic nanoparticle or nanowire directly on the inner wall of the photonic crystal fiber (PCF) [63,75–79], with a typical schematic shown in Fig. 2(a) left panel; (2) to mix the metallic nanoparticle with bioanalyte in a liquid solution for PCF interaction [65–67,80], with a typical schematic shown in Fig. 2(b). The measurement results are shown in the right panel of Figs. 2(a) and 2(b), respectively. The SERS spectra of the R6G molecules with a concentration of 10^{-6} M using a liquid-core PCF (LCPCF) with sealed and unsealed ends are

illustrated in Fig. 2(a) right panel. They are in comparison with the direct sampling, whose enlarged SERS spectrum is included in the inset of the plot. The SERS signal from the sealed fiber structure is around 100 times stronger than that from the direct sampling, which is contributed by the surface enhancement from the silver NP and the LCPCF design. Figure 2(b) right panel shows the SERS spectra of the protein cytochromec detected by bulk solution and a tip-coated multimode fiber (TCMMF) probe at a concentration of 0.2 μg/mL. It shows that the TCMMF probe can achieve an LOD of 0.2 μg/mL, which is an order of magnitude lower than that of bulk detection. This is due to the enhanced electromagnetic field from the SERS substrate on the TCMMF probe.

For both approaches mentioned above, the PCF air cavity can either be in the core of the hollow-core fiber (HCF) or the cladding of the solid-core fiber (SCF). The LOD of the SERS-based fiber sensor is determined by the spatial overlap between the optical mode and the analyte solution. Therefore, the LOD is found to be generally lower for the case where the mixed solution is confined within the HCF core [21] due to higher spatial overlap with the optical mode (e.g., 10^{-10} M of LOD in Ref. [80]), compared with the SCF case where the mixed solution interacts with the evanescent wave of the optical mode within the cladding area of the fiber (e.g., 10^{-7} M of LOD in Ref. [79]). The cross section of the above-mentioned HCF achieving 10^{-10} M LOD is shown in the inset of Fig. 2(c). The measurement result presented in Fig. 2(c) shows the SERS spectrum from the detection of 10^{-10} M R6G using liquid solution to fill the core of the HCF. The liquid solution is a mixing of R6G and silver NPs. The spectrum peaks are marked from (a) to (l) as shown in the figure. The peaks (a) and (c) are contributed by the silver NPs, and the rest peaks are R6G peaks. One more point worth mentioning is that the LOD on the level of 50 fM is achieved by using the side-channel PCF through the significant increase of the interaction area between liquid samples and the guided light wave within the fiber core [68]. The SERS spectra of different R6G concentration solutions are illustrated in Fig. 2(d). The fiber cross section is shown in the inset of Fig. 2(d). The detection limit of 50 fM R6G concentration solution can be confirmed by
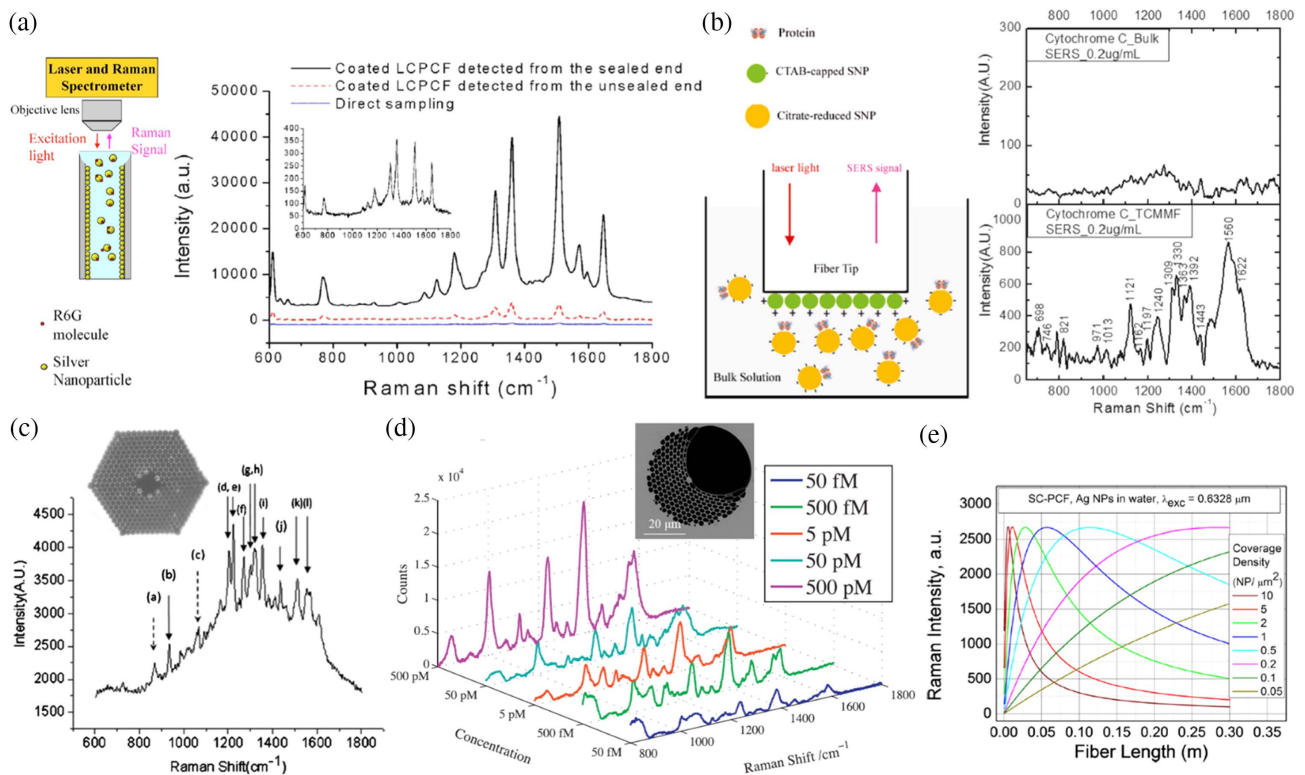
Fig. 2. SERS-based fiber biosensors. (a) Left: schematic of the SERS-based fiber optic biosensor with metallic nanoparticle coated on the inner wall of PCF. Right: SERS spectra of R6G molecules with concentration of 10^{-6} M, comparing the cases among the direct sampling and coated LCPCFs. (Adapted from [75] with the permission of AIP Publishing.) (b) Left: schematic of the SERS-based fiber optic biosensor utilizing bio-analyte and the metallic nanoparticle solution. Right: measured SERS spectra of 0.2 µg/mL cytochrome C solution by using bulk solution and TCMMF. (Adapted with permission from [65]. Copyright 2011 American Chemical Society.) SNP is short for silver nanoparticles. CTAB is short for cetyltrimethylammonium bromide. (c) SERS spectrum of 10^{-10} M R6G using liquid solution to fill the core of the HCF. Inset: cross section of HCF, demonstrating LOD of 10^{-10} M. (Adapted with permission from [80]. Copyright Optical Society of America.) (d) SERS spectra under R6G solution with different concentrations. Inset: cross section of channel PCF achieving LOD of 50 fM. (Adapted with permission from [68]. Copyright 2016 Elsevier.) (e) Simulation results investigating how fiber length affects the Raman intensity under different NP concentrations for SERS-based fiber sensor. (Reprinted from [76] with the permission of AIP Publishing.)

Table 2. Summary of Recent SERS-Based Optical Fiber Biosensors

Sensing Mechanism	Functional Material	Excitation Wavelength	Analyte	Detection Type	LOD	Ref.
SERS (fiber facet)	Ag nanodendrites	532 nm	Permethrin pesticide	Backward scattering	0.0035 ppm	[70] (2019)
SERS (hollow fiber tip)	Au@Ag core-shell nanorods and Ag nanospheres assembled layer-by-layer	632.8 nm	Methylene blue; cytochrome C; melamine	Backward scattering	1 fM (methylene blue); 1 µg/mL (cytochrome C); 100 nM (melamine)	[72] (2019)
SERS (soft polymer optical fiber)	Ag NPs	785 nm	R6G and 4-mercaptopyridine	Forward scattering	10^{-7} M (R6G) and 10^{-8} M (4-mercaptopyridine)	[73] (2018)
SERS (two fibers)	Au NPs	785 nm	Rh B	Forward scattering (one fiber for Raman excitation, the other fiber for collection)	<10 ppm	[74] (2018)
SERS (tapered fiber tip)	Ag NPs	785 nm	4-Aminothiophenol (4-ATP)	Backward scattering	10^{-9} M	[71] (2017)
SERS (on side-channel PCF)	Au NPs	632.8 nm	Rhodamine 6G (R6G)	Backward scattering	50 fM	[68] (2016)

the Raman spectrum with notable peaks at 1184 cm^{-1}, 1310 cm^{-1}, 1368 cm^{-1}, and 1575 cm^{-1}, which correspond to the vibration modes of R6G molecules. Also, an even lower LOD of 1 fM is recently reported by coating layer-by-layer assembly of Ag nanospheres and nanorods on the tip of the HCF [72].

In the SERS-based fiber sensor design, the optical mode propagation length is an important parameter. To optimize the Raman signal for sensing, the trade-off between the Raman gain and metallic loss has been investigated [63,76]. It is found that for a metallic NP-based sensor, when the particle density is higher than a certain level, the scattering loss will be dominating over the Raman gain. While for the case when the particle density is lower than that level, the Raman signal can build up along the propagation of the optical fiber. Such a trade-off can be illustrated from the simulation result shown in Fig. 2(e) [76]. In addition, different scattering enhancement mechanisms, such as stimulated Raman scattering [81] and enhanced random scattering [82], can be explored on a fiber platform to achieve better sensing performance in terms of higher sensitivity and lower LOD.

B. Interference-Based Optical Fiber Sensors

1. Bragg Grating-Based Fiber Sensors

The Bragg grating-based fiber makes use of the periodic perturbation to create the phase matching either along the fiber propagation direction or along the fiber radial direction. Therefore, the currently demonstrated Bragg grating-based fiber biosensors can be categorized into the following four types based on grating structure: fiber Bragg gratings (FBGs), tilted fiber Bragg gratings (TFBGs), long-period fiber gratings (LPFGs or LPGs), and photonic bandgap fiber (PBGF). For the FBG type sensor, the gratings create the coupling between the fundamental co-propagating mode and the counter-propagating mode and act as a wavelength selective mirror, whose reflection wavelength is determined by the Bragg condition [83]

$$\lambda = 2n_{\text{eff}}\Lambda, \qquad (1)$$

where λ is the reflection wavelength, n_{eff} is the effective refractive index of the core mode, and Λ is the grating period. This grating period is typically less than 100 μm [22]. For the FBG, the optical mode is not sensitive to the surrounding since it is well confined within the fiber core with a typical diameter of 8 μm. The fiber cladding used to cover the core has a typical diameter of 125 μm. To make the core mode interact with surrounding, the cladding needs to be removed by polishing or etching [84]. The reflected signal from the FBG will experience wavelength shift contributed by the change of effective index from the overlap between the evanescent field and the sensing material outside the fiber core.

The second type of grating-based sensor is to create the coupling between the core and the cladding mode by using the TFBG. Since the cladding modes have lower effective index compared with the core mode, the transmission spectrum of the TFBG will have a few drops at the shorter wavelength compared with the reflected wavelength within the core mode. These shorter wavelengths can be determined by the following modified Bragg condition:

$$\lambda = (n_{\text{eff}}^{\text{core}} + n_{\text{eff}}^{\text{clad}-m})\frac{\Lambda}{\cos\theta}, \qquad (2)$$

where $n_{\text{eff}}^{\text{core}}$ and $n_{\text{eff}}^{\text{clad}-m}$ are the effective index of the core and the mth cladding mode, respectively. θ is the tilting angle of the grating relative to the fiber central axis typically ranging from 4° to 10° [85].

The LPFG type fiber sensor also creates coupling between the fundamental core mode and the cladding mode in the optical fiber. In comparison with the FBG, the grating period of the LPFG-based sensor typically has a range from 100 μm to 700 μm [19,86–88]. The resonant wavelength can be expressed in the following equation:

$$\lambda = (n_{\text{eff}}^{\text{core}} - n_{\text{eff}}^{\text{clad}-m})\Lambda. \qquad (3)$$

Since the resonance wavelength is dependent on the effective refractive index of the m-order cladding mode, the evanescent optical field is able to interact with the surrounding, in comparison with the case of the FBG. A recent review has done a summary on the first three types of grating-based sensors [22]. In the following two paragraphs, the discussion will be focused on the most recent work using graphene oxide (GO) coating on the LPFG as well as the last PBGF type.

An ultrasensitive biosensor with a remarkably low LOD of 0.2 aM was demonstrated recently by an LPFG coated with GO, which has high water dispersibility and high biomolecule affinity [13]. The fiber sensor schematic is shown in Fig. 3(a) top panel. The sensing result is included in Fig. 3(a) bottom panel, showing the sensorgrams. The y axis of the sensorgram represents the ratio between the wavelength shift [unit: nanometer (nm)] and the surrounding refractive index (SRI) sensitivity (unit: nm/RIU), and the x axis represents the analyte concentration. From the figure, it can be observed that when the concentration of the biotinylated bovine serum albumin (bBSA) analyte varies from 0.1 aM to 1 fM, the responses for sensors LPG$_1$ and LPG$_2$ are very close. Both of them have the streptavidin (SA) layer for binding purpose but have different polycarbonate layer thickness. In comparison, the sensor LPG$_3$ has low response to bBSA due to the absence of the SA layer. The selective binding between the SA and biotin can be observed through the response difference between LPG$_1$ (or LPG$_2$) and LPG$_3$.

The PBGF type of sensor achieves the mode confinement by using either the periodic multilayer or photonic crystal structure along the radial direction of the fiber, which differentiates themselves from the previous three types. A polystyrene (PS)/poly-methacrylate (PMMA) multilayered hollow-core structure can be used to form the photonic bandgap [89,90]. This kind of fiber provides a good platform for biosensing contributed by the fact that the biomolecules can be easily bonded to the PMMA surface [10]. A typical fiber cross section is illustrated in Fig. 3(b) top panel. A thin layer of polyvinyl butyral (PVB) film with a thickness of 500 nm is coated on the inner surface of the fiber core. The dissolution dynamics of PVB has been monitored to demonstrate the surface sensing modality. The result is shown in Fig. 3(b) bottom panel. At first, the reference spectrum was taken at the beginning when 16 wt.% NaCl solution in water was used. The solution has the same refractive index as ethyl alcohol and is chemically inert. Then the ethyl
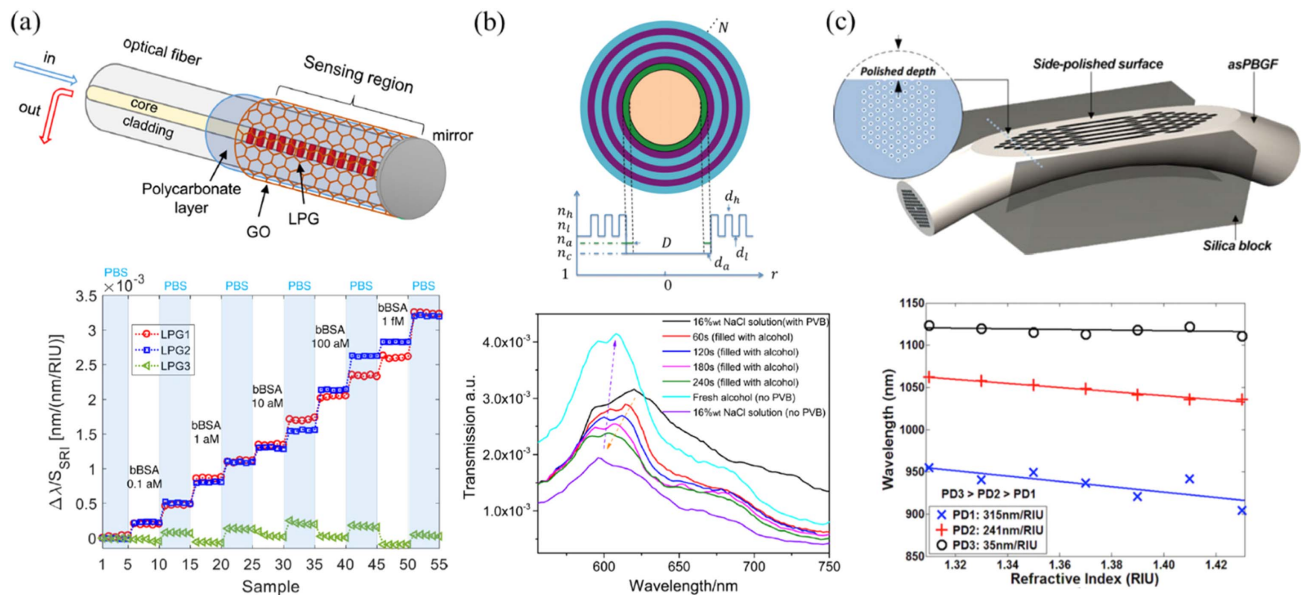
Fig. 3. Bragg grating-based fiber sensors. (a) Top: schematic of grating-based fiber sensors with LPBG using GO coating to achieve ultrasensitive detection. Bottom: sensorgram showing wavelength shift normalized to SRI sensitivity under different analyte concentrations for three sensors. (Adapted with permission from [13]. Copyright 2018 Elsevier.) (b) Top: cross section of PBGF with PS/PMMA multilayer structure. Bottom: transmission spectra of PBGF during the PVB layer dissolution process. (Reprinted with permission from [89]. Copyright Optical Society of America.) (c) Top: schematic of side-polished PBGF. Bottom: the PBGF wavelength shift with respect to refractive index change for three different polishing depths (PDs). (Reprinted with permission from [91]. Copyright 2012 IEEE.)

alcohol was introduced into the fiber, and the PVB analyte layer was dissolved. The transmission spectra were taken every minute and plotted in the figure. As the PVB layer was dissolved, the transmission spectrum shifted to the shorter wavelength. A surface sensitivity of 0.052 nm/nm can be obtained from the wavelength shift with respect to the layer thickness change. In addition, the surface sensitivity has been increased to 0.07 nm/nm by squeezing a section of the fiber, due to the increase of the overlap between the core-guided modes and the analyte layer.

An alternative PBGF structure is using a photonic crystal SCF. The sensing functionality can be realized by side polishing to form the D-shaped cross section [91], with a schematic illustrated in Fig. 3(c) top panel. The sensing result is shown in Fig. 3(c) bottom panel, illustrating the blueshift of the PBGF wavelength with respect to refractive index change under three different polishing depths (PDs). Both PD1 and PD2 demonstrate a sensing resolution of 10^{-5} RIU. By comparing the gradient of the fitted curve for PD1, PD2, and PD3, we can see that the PD3 (with high polishing depth) has the lowest sensitivity. This might be contributed by the damage of the fiber microstructure, which introduces higher fiber transmission losses and results in the reduced sensitivity to index change. In addition, the selected recent works within the past 5 years on grating-based optical fiber biosensors, including FBG, TFBG, LPFG, and PBGF, are summarized in Table 3.

2. Interferometry-Based Optical Fiber Sensors
An interferometer works based on the superposition of multiple optical modes. Depending on the phase relation among multiple signals from different optical paths, the transmission and

attenuation bands can be formed [22]. The fiber-based interferometer can be categorized into two types: transmissive and reflective fiber interferometers.

The structure of the transmissive type can be formed by splicing three fiber segments, including SMF, a fiber-based cavity for optical interference (e.g., an MMF [92,93]), and then SMF. A typical schematic is shown in Fig. 4(a), where MMF is used as a cavity for optical interference. In the sensor, the optical mode couples from SMF to MMF and then couples back to SMF. To enhance the sensitivity of the sensor, etching, polishing, and thin film deposition can be applied to the middle fiber segment [92–95]. The schematic in Fig. 4(b) left panel illustrates the concept of etching the cladding of the MMF to enhance the optical mode interaction with the analyte. The measurement result of sensing anti-IgG analyte with different concentrations is illustrated in Fig. 4(b) right panel. The interference wavelength shift can be observed when the concentration varies from 4 mg/L to 200 mg/L. The Hill equation fitting of the wavelength shift data gives an LOD of 0.2 mg/L (or 200 ng/mL) [92].

Besides using MMF, other ways to create an interferometric structure for mode beating include implementing the following fiber segments between the two fiber pigtails: PCF [9], misaligned fiber [96,97], tapered fiber [98,99], and noncore fiber (NCF) [14]. The schematic of the misaligned fiber is shown in Fig. 4(c) top panel. It is formed by a section of SMF fusion spliced between two sections of SMF with a core offset of 62.5 μm. Its sensing measurement result is shown in Fig. 4(c) bottom panel, with the inset illustrating the linear fitting curve in a low analyte (human IgG) concentration range from 0.5 μg/mL to 5 μg/mL. Based on the measurement results, the

Table 3.   Summary of Recent Grating-Based Optical Fiber Biosensors

Sensing Mechanism	Functional Material	Wavelength	Analyte	Sensitivity	LOD	Ref.
FBG	Graphene oxide	–	C-reactive protein	20.15 pm for 1 mg/L CRP	0.01 mg/L	[84] (2015)
FBG	Aldehyde group and antibody	1559 nm	*Escherichia coli* bacteria	25 pm for 1:100 *E. coli* bacteria diluted in DI water	–	[100] (2017)
TFBG + SPR	Au film	~1545 nm	Glycoprotein	2.867 dB/(mg/mL)	15.56 nM	[101] (2017)
TFBG + SPR	Au film	~1543 nm	Cytokeratin 17	1.5 dB amplitude shift at 10^{-10} g/mL	10^{-12} g/mL	[102] (2017)
LPFG	Polycarbonate-GO multilayer	1300–1650 nm	Biotinylated BSA (bBSA)	2000 nm/RIU	0.2 aM	[13] (2018)
LPFG	Silica-titania film	1560–1570 nm	Anti-IgG	7000 nm/RIU	0.025 mg/L	[86] (2017)
PBGF	PS/PMMA multilayer	550–750 nm	Polyvinyl butyral dissolution dynamic in liquid	0.07 nm/nm (surface spectral sensitivity)	–	[89] (2016)
PBGF	PS/PMMA multilayer	600–800 nm	Liquid analyte solution	1850 nm/RIU	–	[90] (2019)

LOD of the sensor can be obtained as 47 ng/mL. Figure 4(d) shows the schematic of the NCF-based sensor and the sensing result. From the schematic, we can see that the nickel ions on the surface of the NCF can bind the analyte for sensing purpose. The sensing result illustrates the wavelength shifts with respect to the analyte concentration variation. The experimental data is fitted by using the Langmuir isotherm model, from which the LOD can be obtained as 0.8368 ng/mL. It is
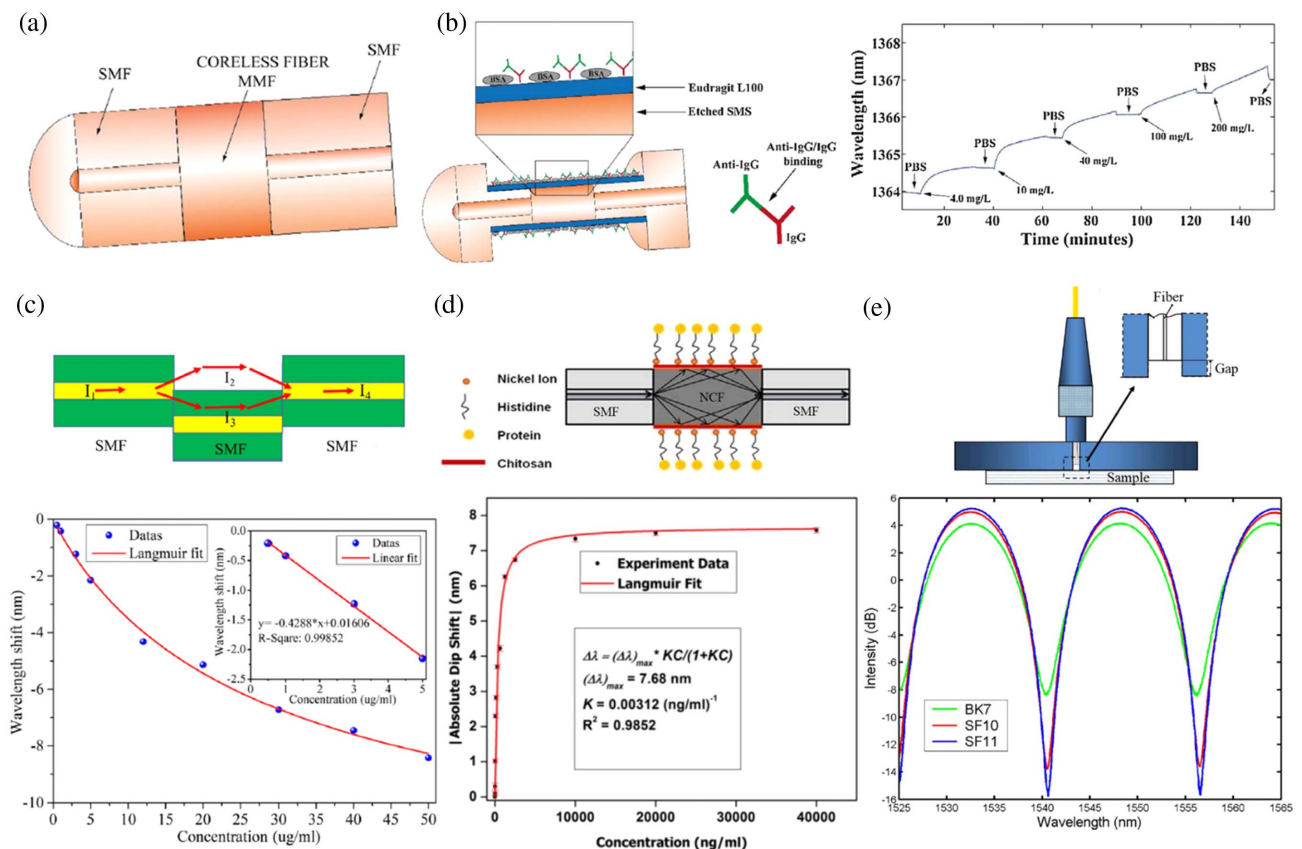

Fig. 4.   Interferometer-based optical fiber sensors. (a) Schematic of fiber with SMF-MMF-SMF structure for the interferometry-based sensor. (b) Left: schematic of interferometry-based fiber sensor with SMF-etched MMF-SMF. Right: sensing result of wavelength shift corresponding to different concentrations of goat anti-IgG from 4 mg/L to 200 mg/L. (Adapted with permission from [92]. Copyright 2018 Elsevier.) (c) Top: schematic of the fiber sensor with SMF-misaligned fiber-SMF. Bottom: sensing measurement data showing wavelength shift with respect to the analyte concentration. The measurement data is fitted by Langmuir isotherm curve. Inset: the linear fitting curve in a low analyte concentration range from 0.5 to 5 μg/mL. (Adapted with permission from [96]. Copyright 2018 Elsevier.) (d) Top: schematic of the fiber sensor SMF-NCF-SMF structure. Bottom: sensing measurement result showing the absolute wavelength shift with respect to the analyte concentration. (Adapted with permission from [14]. Copyright 2018 Elsevier.) (e) Top: schematic of the interferometry-based sensor with the FP cavity external of the optical fiber. Bottom: measured reflection spectra from the samples with different refractive indices. (Adapted with permission from [103]. Copyright Optical Society of America.)

Table 4.　Summary of Recent Interferometer-Based Optical Fiber Biosensors

Sensing Mechanism	Functional Material	Wavelength	Analyte	Sensitivity	LOD	Ref.
SMF-etched MMF-SMF	Eudragit L100 and IgG	1360–1380 nm	Anti-IgG	280 nm/RIU	200 ng/mL	[92] (2018)
SMF-PCF-SMF	– (fiber surface modification for immobilization)	1535–1550 nm	Antigen bovine serum albumin	722.3 nm/RIU	125 pg/mL	[9] (2017)
SMF-tapered SMF-SMF	Biomarker antibody	1510–1560 nm	Breast cancer biomarker (HER2)	2333 nm/RIU	2 ng/mL	[98] (2017)
SMF-misaligned SMF-SMF	Staphylococcal protein A, goat anti-human IgG	1300–1700 nm	Human-IgG	13936 nm/RIU	47 ng/mL	[96] (2018)
SMF-NCF-SMF	Chitosan (CS)-nickel (Ni) film	1570–1610 nm	Hexa-histidine tagged microcin	0.0308 nm/(ng/mL)	0.8368 ng/mL	[14] (2018)
MMF-FP	–	1530–1570 nm	Water-glycerin mixture	5.49 nm/RIU	–	[104] (2018)

worth mentioning that a record low LOD of 125 pg/mL was reported contributed by the modified fiber surface with a high affinity toward a specific protein [9]. In addition, the length of the middle segment can also be optimized to achieve high sensitivity and low LOD [96].

Alternatively, the reflective interferometer can be formed by a Fabry–Perot (FP) cavity through the backreflection from two interfaces. These interfaces can either be internal [104,105] or external [103] of the optical fiber. In Ref. [104], the internal FP cavity is formed by the backreflections from different surfaces of the microbubble created by the arc on the fiber splicing machine. In the meanwhile, the external FP cavity can be formed by the backreflections from the surface of the fiber facet and the sample with an air gap in between. The schematic is shown in Fig. 4(e) top panel. The spectra of reflected signal from glass samples with different refractive indices are shown in Fig. 4(e) bottom panel. From the fringe contrasts, the refractive index of the sample can be calculated. The FP-based fiber interferometer has the advantage of low cost, compactness, and ease of implementing analyte for biomedical applications [106,107]. FP structure-based fiber sensors are used to detect BSA with the LOD reported to be 0.48 ng [106], and measure liposome with a concentration range from 2.5 mM to 10 mM [107]. Also, the selected recent works within the past 5 years on interferometer-based optical fiber biosensors covering all the structures mentioned above are summarized in Table 4.

3. FIBER PROBES FOR BIOIMAGING

In this section, various fiber-based technology development is reviewed to improve the image quality and miniaturization for *in vivo* applications. At the end of the section, future directions are given based on new exciting emerging technologies that have been demonstrated for other fields and have the potential to be applied in the bioimaging field. Note that fiber-based imaging systems that did not demonstrate biomedical applications are not included.

A. Optical Bioimaging
Many optical bioimaging techniques, especially endoscopes, are based on fibers with their capabilities to transmit, reflect, and scatter light. Imaging techniques based on the light at the far field, such as optical coherence tomography (OCT), multipho-

ton microscopy, and nonlinear Raman scattering microscopy, will be introduced with the focus on how the development of optical fibers helps to improve the image resolution. However, the light at the far field is being affected by diffraction, which is a fundamental property of light. Hence, the resolution cannot go beyond the diffraction limit. Near-field imaging techniques capture the sample image at the near field by using the evanescent wave of the light before it propagates to the far field and hence, the resolution is not affected by the diffraction.

Fiber-based imaging with a high spatial resolution is controlled by the confinement of the light field in the fiber core, which is closely related to the PCF design parameters, e.g., core diameter, pitch size, and refractive index contrast between the core and the cladding. It has been shown that the effective mode area is

$$A_{\mathrm{eff}} = \frac{(\int |E|^2 \mathrm{d}A)^2}{\int |E|^4 \mathrm{d}A} = \frac{(\int I \mathrm{d}A)^2}{\int I^2 \mathrm{d}A}, \qquad \textbf{(4)}$$

where E is the electric field amplitude and I is the optical intensity. The mode radius is $w = \sqrt{A_{\mathrm{eff}}/\pi}$. It is sensitive to the above-mentioned PCF parameters. In Ref. [108], the authors plotted the effective radius of a PCF mode as a function of the core diameter (d) and the pitch size (Λ). A larger d/Λ ratio leads to a higher spatial resolution of a fiber probe. For example, with a ratio of 0.9, the minimum core size can reach $w = 0.2\lambda$. Hence, a detailed understanding of the physical parameters of PCF designs can provide unique properties in imaging and microscopy applications.

1. Optical Coherence Tomography (OCT)
OCT is a noninvasive imaging technique that was developed in the early 1990s and was since successfully applied in biomedical diagnosis. Because it can achieve micrometer resolution at millimeter depth within a scattering medium, such as biological tissue, it is widely used in ophthalmology and optometry to obtain detailed images from the retina. It has also been used in head and neck, cardiology, and dermatology clinical diagnosis. Specifically, the use of fiber optics enables the OCT imaging of internal organs. OCT uses low-coherence light interferometry configuration and detects the change in the refractive index of the sample. The input light is divided into two arms, a sample arm (attached to a tissue sample) and a reference arm (attached to a movable reference mirror). The reflected light

from the two arms recombines and forms an interference signal only when the optical path lengths of the two arms are matched within the coherence length of the input light. Depth scanning is achieved by moving the reference mirror.

It has been shown that the image resolution in the axial direction is proportional to the wavelength of the input light (λ) and inversely proportional to the bandwidth of the input light ($\Delta\lambda$) [109]. Hence, a light source with a small λ and large $\Delta\lambda$ is desired to achieve a high image resolution, i.e., small Δx. Optical fibers can help increase $\Delta\lambda$ of light sources. *In vivo* imaging of the cornea and anterior segment with a resolution of 6.5 µm and a sensitivity of 119 dB was demonstrated. OCT systems operating at a center wavelength of 1.7 µm were also developed [109]. An all-fiber-based system was generated by a normal-dispersion highly nonlinear fiber with a femtosecond ultrashort pulsed Er-doped fiber laser as the seed source. A large-mode-area PCF and a polarization-maintaining fiber were also used for dispersion compensation. *In vitro* OCT images showed an ultrahigh resolution of 3.3 µm and a sensitivity of 95 dB.

Another way to improve resolution is to focus the light coming from the fiber by adding a focusing element directly on the fiber facet or in the light pathway before reaching the sample (e.g., tissues). Graded-index (GRIN) lenses and ball lenses are widely used options as focusing elements. GRIN lenses have been fused onto SMF and PCF [110] for *in vivo* microscopic brain motion measurements and biological sample imaging with a working distance of up to 1270 µm and resolution of 14.2 µm, which are comparable to the values obtained by using a conventional objective lens. Not only GRIN lenses, researchers have also tried to attach a sapphire ball lens at an SMF tip with an air gap [working distance (WD) = 415 µm, resolution = 11 µm] or an ultraviolet epoxy spacer (WD = 1221 µm, resolution = 18 µm). Because of the high refractive index of sapphire ($n = 1.75$), high focusing power and lateral resolution were achieved even when the probe was submerged in the vitreous gel. Ultrahigh sensitivity up to 88 dB OCT fiber probe was applied for corneal and retinal imaging [111].

The latest trend is to adopt nanotechnology into the development of nanoendoscopic OCT for better imaging performance than GRIN lenses and ball lenses. A new type of nano-optics endoscopic OCT probe was recently developed based on metasurface which tackles the spherical aberration and chromatic aberration [112]. The metasurface is an assembly of nanostructures capable of manipulating light properties such as amplitude, phase, and/or polarization at sub-wavelength precision. In particular, a metasurface lens (metalens) is a type of metasurface that functions as a lens but is ultrathin and flat [113]. A metalens was attached to a prism on an SMF facet encased in an OCT catheter and achieved near-diffraction-limited focusing resolution and high depth of focus. Endoscopic OCT imaging in resected human lung specimens and in sheep airways *in vivo* was demonstrated using the probe.

2. Nonlinear Optical Imaging

Multiphoton (or two-photon) excitation microscopy is a fluorescence imaging technique that utilizes a nonlinear process whereby a fluorophore is excited by two or multiple infrared photons (typically 700–1000 nm) and emits a single photon of higher photon energy in the visible spectrum (typically 400–500 nm). Because infrared light can penetrate deeper into the tissue and cause less photodamage, it has advantages over the confocal microscopy using single-photon excitation. However, two or multiple photons need to be absorbed simultaneously. The probability of fluorescence emission increases dramatically with the excitation intensity, so femtosecond lasers are required which are much more expensive than the continuous wave lasers used in confocal microscopy.

Three-dimensional two-photon excitation microscopy endoscopic imaging *in vitro* of a gastrointestinal tract tissue and a human breast cancer tissue was demonstrated [114,115]. The imaging system consists of a double-clad PCF (DCPCF), a GRIN lens, and a two-axis microelectromechanical system mirror. The DCPCF consists of a large core surrounded by two cladding layers. The excitation light propagates in the core region and the collected fluorescence light propagates in the cladding, which supports multimode [see Figs. 5(a)–5(c)]. In this way, both the excitation and collection efficiencies are increased. The penetration depth was approximately 100 µm and the axial resolution was 10 µm. A similar and improved
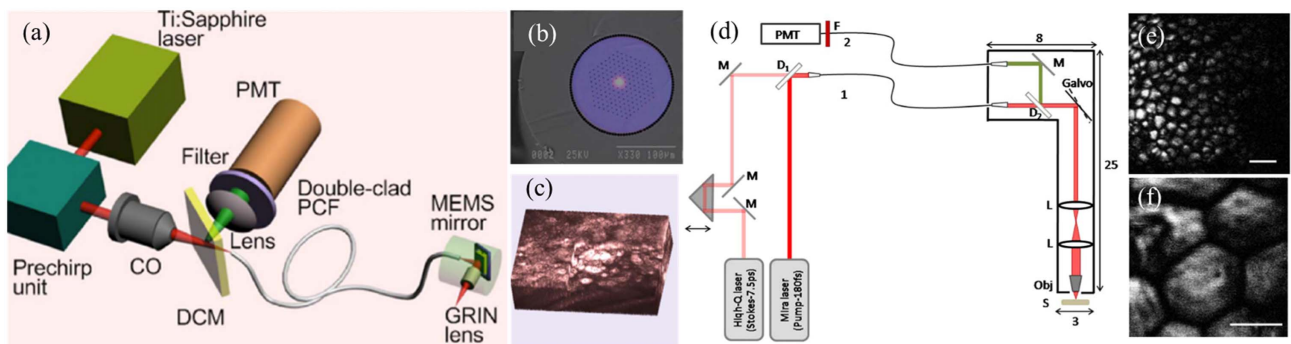

Fig. 5. Nonlinear bioimaging techniques. (a) Schematic of a two-photon fluorescence endoscope. (b) Scanning electron microscopy (SEM) image of a DCPCF overlaid with the light output patterns: single-mode propagation in the core at 800 nm and multimode propagation in the inner cladding at 410 nm. (c) 3D visualization of the human breast cancer tissue imaged using system in (a). [(a)–(c) reprinted from [115] licensed under CC BY 4.0.] (d) Schematic of a fiber-probe based CARS imaging system. Fiber 1 was used for delivery of the excitation pulses and fiber 2 was used for detecting the CARS signal from the sample. (e) CARS image of small adipocytes of mouse ear skin. (f) CARS image of adipocytes of the subcutaneous layer of rabbit skin. Scale bar is 50 µm. [(d)–(f) reprinted with permission from [116]. Copyright Optical Society of America.)

configuration based on DCPCF was reported [117]. Besides DCPCF, a hollow-core PCF was also used for two-photon fluorescence imaging. A miniaturized two-photon fluorescence endoscopy was demonstrated [118]. It was composed of a PCF for light delivery, an MMF for light collection, a high-numerical-aperture (NA) GRIN lens for focusing, and a two-axis piezo scanner system for scanning. It achieved an axial resolution of 5.8 μm with a field of view 420 μm × 420 μm for imaging mitochondria. A major problem with the fiber-based two-photon imaging technique is the small aperture of the fiber probes limiting the collection efficiency of the fluorescent signal. To solve this problem, solutions based on DCPCFs have been proposed. In Ref. [119], the short pulse excitation signal passed through the inner single-mode core and the fluorescent signal was collected through a high-NA multimode outer core (NA > 0.65 at the fluorescent wavelength). In this way, both the excitation and collection efficiencies were kept high. It was shown that an order of magnitude improvement over the conventional SMF or MMF can be achieved. A modified version of this experiment was reported in Ref. [120] through a guided-wave mechanism. Here, when the PCF probe was brought in contact with the target molecules, a few nanoliters of two-photon excited molecules filled the air holes in the fiber cladding and were interrogated with the evanescent field of the PCF waveguide modes. The fluorescent signal detected in this way showed a 2 order of magnitude improvement over that in Ref. [119]. Experiments were done with an R6G dye and the Alexa Fluor family of dyes, which are commonly used in cell biology, fluorescent microscopy, and green fluorescent protein.

Coherent anti-Stokes Raman scattering (CARS) is another nonlinear optical modality that has a growing interest. Different from multiphoton fluorescence imaging, which is induced by a single laser pulse, CARS imaging requires two pulses with different wavelengths. Because the CARS signal is coherent, it is orders of magnitude stronger than the Raman signal, which is spontaneous emission. There are three frequencies of interest: a pump beam with frequency w_p, a Stokes beam of frequency w_s, and a probe beam with frequency w_{pr}. The output anti-Stokes frequency will be $w_{pr} + w_p - w_s$. This gives rise to design challenges such as how to suppress the optical nonlinearities in the delivery fiber and how to effectively collect the backward-scattered signal in the detection fiber [116]. Three types of fibers were investigated for light delivery, including an SMF, a DCPCF, and a large-mode-area PCF. The large-mode-area PCF was chosen for light delivery with minimal spectral broadening effect and a large-mode-area MMF was chosen for maximum signal collection. Examples of CARS imaging of the mouse ear skin, the rabbit skin tissues, and the meibomian gland in mouse *ex vivo* are shown in Figs. 5(d)–5(g). Another challenge is how to tailor the short-pulse laser excitation source spectrally and temporally. PCFs were used to address this problem [121,122]. For example, a PCF was used to generate a frequency-tunable Stokes source through a soliton self-frequency shift. By varying the power of laser pulses launched into the PCF, the soliton output from the PCF was tuned from 1.35 to 1.75 μm. The dispersion, nonlinearity, and length of the PCF were carefully designed to

match the input laser pulse parameters. The efficiency of energy conversion of these PCFs was 15%. Experiments with mouse brain were carried out and CARS spectra were taken [15]. By studying the peaks of the lipid symmetric C-H stretch vibrational mode and the symmetric and asymmetric H_2O stretch vibrational modes, it was shown that the system was able to distinguish two regions in the mouse brain with different lipids and water contents and orientation. This will help distinguish the white matter from the gray matter in the mouse brain tissues.

3. Near-Field Optical Microscopy

In scanning near-field optical microscopy (SNOM), the incident light is focused through an aperture, usually a fiber tip with a diameter smaller than the wavelength generating evanescent waves that are nonpropagating and only exist in the close distance to the aperture. The sample is placed in the near-field regime of the light and imaged by a detector which is mounted on a piezoelectric stage for raster scanning to form an image. The spatial resolution of SNOM is not dependent on the incident wavelength, but only on the length of the aperture or the diameter of a microscopic probe tip, e.g., a tapered fiber tip. Hence, the ability to fabricate a high-quality small-diameter fiber tip is important. In the review [123], the authors summarized several fabrication techniques including grinding and polishing, chemical etching, thermal pulling, focused ion beam milling, femtosecond laser machining, electron-beam lithography, nanoimprinting lithography, and photopolymerization methods, etc.

A hybrid system combining an SNOM tip attached to a conventional inverted optical microscope was built [124]. It was used to image fibroblasts sub-surface cellular structures at 250 nm resolution and 100 nm depth. It was also used to image the fragile chromosomes at 100 nm resolution. In another example, SNOM was combined with atomic force microscopy (AFM) to provide nanoscale fluorescence imaging of single amyloid fibrils [125]. The SNOM probe is a metal-coated tapered fiber tip having an aperture of 100 nm. The sample was imaged at the near field approximately 10 nm below the fiber tip. Fluorescent signals generated from fibrils were collected by a microscope objective and an avalanche photodiode and used as the feedback signal for AFM topological structural imaging. The study of amyloid fibril formation is helpful in a variety of human diseases diagnoses.

Another arm of near-field imaging is using a microsphere as a tool to transfer the near-field image to the far field and the image was captured by a fiber or an objective. It is often called a near-field nanoscope. A biomaterial-based near-field nanoscope constructed by trapping a cell on a fiber tip was recently developed [126]. Unlike nanoscopes that are made of inorganic materials, nanoscopes that are made of biomaterials suffer from intrinsic small refractive index contrast that limits their performance as high-resolution imaging devices. The authors overcome this by having a spherical-shaped cell (termed a "bio-magnifier") semi-immersed in a suspension and combining with the interference effect from the reflection of a mirror substrate. A sub-diffraction light spot and focusing were achieved. Human epithelial cells were used as imaging samples. A resolution of 100 nm ($\lambda/5.5$) was achieved at a scanning rate of

20 μm/s. Moreover, the focal length could be tuned from 0.7 μm to 5 μm by varying the shape of the biomagnifier.

B. Acoustic Bioimaging

Ultrasound imaging uses sound waves or acoustic waves to view the internal organs, monitor heart rates, and examine baby growth in expectant mothers and for other nonmedical applications. Compared with optical bioimaging, acoustic waves can penetrate much deeper into the tissue, but the resolution is poorer. Two important parameters of ultrasound transducers are high sensitivity and large bandwidth. Unfortunately, most commonly used piezoelectric transducers based on the piezoelectric effect face this challenge of the inherent trade-off between sensitivity and bandwidth. Hence, researchers have proposed to use optical methods to generate and receive ultra-

sound as an effective alternative to overcome this challenge. In addition, optical methods based on optical fibers offer the additional benefit of being a small footprint for minimally invasive endoscopic ultrasound.

A comprehensive review paper was published to summarize the technology development in the laser-generated ultrasound (LGUS) as well as optical detection of ultrasound as an all-optical ultrasound imaging platform [127]. For ultrasound generation, it is mainly based on the photoacoustic effect where materials absorb incident light and generate ultrasound [see Fig. 6(a)]. Widely used light-absorbing materials are carbon nanotubes and gold nanoparticles attached at the fiber tip. For ultrasound detection, it is mainly based on resonant cavities such as FP cavities, Bragg gratings, and microring resonators. The first two have been applied in the fiber context.
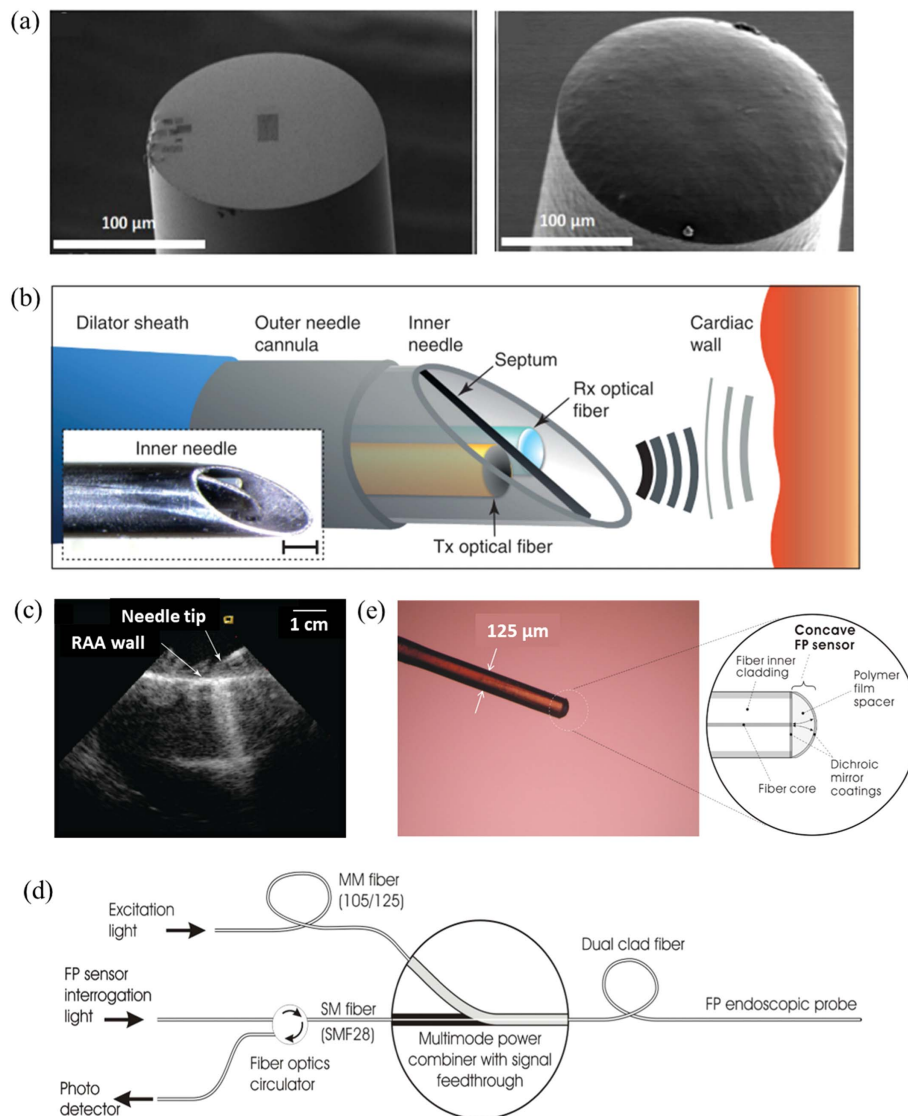

Fig. 6. Fiber probes for acoustic bioimaging. (a) SEM images of carbon nanotubes and gold nanoparticles as the light-absorbing materials attached at the fiber tip for LGUS. (Adapted from [128] licensed under CC BY 4.0. Adapted with permission from [129]. Copyright 2014 AIP Publishing.) (b) All-optical ultrasound imaging based on fibers encased in a needle for interventional imaging. (c) The needle tip was positioned at the right atrial appendage wall with imaging depths extended more than 1 cm into the tissue. [(b) and (c) adapted from [130] licensed under CC BY 4.0.] (d) Schematic of the all-optical endoscopic imaging system with a dual clad fiber. (e) Photo of the concave cavity FP sensor probe. [(d) and (e) adapted with permission from [131]. Copyright 2011 SPIE.]

The earlier development was based on FBG. Bragg gratings are used to selectively reflect the light of a certain wavelength (λ_B) with high sensitivity. Since λ_B is sensitive to perturbations of the grating structures, FBG can be used for pressure (e.g., caused by acoustic waves) and temperature sensing [132]. The change in λ_B due to the strain caused by ultrasound was measured electrically by a radio frequency spectrum analyzer. However, it was found that the grating was subject to a non-uniform strain, i.e., a portion of the grating was modulated while another portion was unmodulated, which made the system response complex. To make it an effective ultrasound probe, the authors concluded that the grating length should be less than half of the acoustic wavelength in fused quartz, which limits the acoustic frequency detection range. It was further suggested that proper desensitization of the fiber is helpful.

Detecting ultrasound signals by using FP cavities has also attracted attention recently. Acoustic waves incident on the FP cavity will cause a change in the cavity characteristics which can be detected by the reflectivity change of the interrogation light beam. An all-optical ultrasound imaging probe based on optical fibers was developed and used for interventional imaging for the first time [130]. Two optical fibers separated by a metal septum for acoustic isolation were encased in a cardiac needle for *in vivo* imaging [see Figs. 6(b) and 6(c)]. The optical transmitter is an MMF with one end coated with multiwalled carbon nanotube-polydimethylsiloxane for ultrasound generation. The optical receiver is an SMF with an FP cavity attached at one end. A preclinical swine study was conducted. The needle was able to image the dynamic movement of a beating heart at a 50 Hz scan rate at a depth of 2.5 cm with an axial resolution of 64 μm. An improved FP cavity design based on a planar–concave optical microresonator was proposed to improve the performance [133]. A tightly focused interrogation light beam was incident on the planar side and diverged as it propagated inside the cavity, but the divergence was perfectly matched with the concave side which refocuses the beam and prevents the beam from any lateral position shift. As a result, a high Q value of greater than 10^5 was achieved corresponding to large bandwidth and high sensitivity, i.e., low noise-equivalent pressure. All-fiber-based 3D pulse-echo ultrasound imaging of *ex vivo* porcine aorta was performed. The sensor bandwidth is 55 MHz (tunable by the cavity thickness). The axial and lateral resolutions are 94.2 μm and 65.9 μm, respectively. Other references based on FP cavities are, for example, Refs. [134–136].

Photoacoustic imaging (PAI) is based on the photoacoustic effect where pulsed light energy was absorbed by the sample and converted to thermal energy causing the transient thermal expansion motion and emission of ultrasound waves in the megahertz range. The ultrasound signals are detected by ultrasound transducers and are proportional to the absorbed light energy. Hence, by studying the emitted ultrasound signal strength, one can obtain the optical contrast information of different samples. Photoacoustic imaging uses light as the excitation and sound as the detection, so the imaging resolution and depth are in between optical imaging and acoustic imaging techniques. It has been used in medical applications including functional brain imaging [137,138], breast cancer [139], tumor margin detection [140], and skin diseases such as nonmela-

noma skin cancer detection [141] and psoriasis [142]. Optical fibers can play a role in PAI in three areas: the light source, the light delivery, and ultrasound detection. Similar to all-optical ultrasound imaging, an all-optical-based photoacoustic imaging probe was proposed [131]. The fiber was a dual-clad 1550 nm SMF, where the core area was used for ultrasound detection and the inner multimode cladding was used for excitation light delivery [see Figs. 6(d) and 6(e)]. The ultrasound detection principle was based on the FP cavity similar to the one in Ref. [133]. A variety of phantom studies were conducted to demonstrate the potential applications for endoscopic imaging. This approach presents the minimum possible photoacoustic probe that can be achieved, i.e., the diameter of a single fiber (~200 μm).

4. FIBER PROBES FOR OPTICAL STIMULATION

In recent decades, there has been a lot of interest to explore the potential capabilities to optically stimulate cells, control the neurons activeness, and simultaneously monitor the neural activity. Compared with the established electrical and magnetic stimulation, the optical approach can confine the light in regions with micrometer scale and hence achieve better performance in terms of higher spatial resolution, targeting precision, and biological specificity. However, implanting solid-state light sources (light-emitting diodes or laser diodes) directly into the region of interest would cause tissue damage after large-area exposure or long-time illumination. Several prototypes have been built as alternative approaches to deliver light to the biological specimen through flexible optical fiber. The term "optrode" was used in analogy to "electrode" to describe the fiber probe for optical stimulation. This section specifically describes several configurations of fiber probes in such an application scenario.

A. Flat Distal End Fiber Probe

The most common configuration is a flat distal end fiber probe [143]. Once the fiber delivers the light (either coherent or non-coherent) into the target tissues, electrodes in the proximity location could conduct *in vivo* recordings of neuron activities [144]. This can determine how optical stimulation affects the local field potentials during the experiment. A benefit from the development in microtechnology, integration of optical fibers with microelectrode, could be realized as shown in Ref. [144]. More sophisticated probe designs were realized to combine three key functions for neuro-study, namely microchannels for chemical delivery/injection, optical waveguides/fibers for light stimulation, and electrode contacts for detection [145,146].

Due to the implantation nature of the device, the heat performance is always a concern for laser beam delivery. Through Monte Carlo simulations, Shin *et al.* calculated the optimized fiber-to-target distances by controlling the light intensity [147]. By considering the bioheat model, the analysis provided a guideline to design a fiber probe in an optogenetics experiment to avoid over-/under-illumination of the light-sensitive proteins.

B. Angled Fiber Probe

Extending the design freedom of the fiber probe from a flat distal end to structures varying in propagation direction is a

trend. One of the typical cases is the angled fiber probe [148]. By side-firing, the polished or cleaved angle becomes another parameter to control the illumination direction. Through numerical simulation, the angle of side-firing can be optimized [149]. The experimental results show that a 38° angle polished fiber tip has the best radiant energy for the infrared wavelength. As illustrated in the fluorescence detection, the single fiber approach offers compactness, compared with the configuration of using separate fibers for light delivery and detection.

For some applications, it is required not only to deliver the light to the side, but also to focus the beam onto the tissues. Tan *et al.* designed a smart needle, as shown in Figs. 7(a) and 7(b) [150]. The ball-shape focusing lens was fabricated at the end of the coreless fiber via a commercial fusion splicer. The focal distance and the emission beam spot size at the focal plane were mainly determined by the curvature of the ball lens. In the work, the ball lens was designed to have a focal length of ~400 μm to ensure the positioning of the focal plane outside the catheter sheath and in the surrounding tissue. The designed sagittal and tangential radii of the ball lens were 75 μm and 100 μm, respectively. After that, the ball lens was further polished at an angle of 36°. The total internal reflection of the incident beam enables the side-viewing catheter design as shown in Fig. 7(a).

Reflective coatings could be applied on the angle cleaved fibers to steer the beam direction. Tamaki *et al.* designed a fiber tip to be inserted in a tube-shaped probe for optical stimulation of neurons and electrical signal recording at arbitrary depths [151]. The silica-based MMF with a core diameter of 50 μm was cleaved at an angle of 45° and a thin layer of Al/Cr film was sputtered on the angle-cleaved surface to make sure the optical stimulation was in the vertical direction, as shown in Figs. 7(c)–7(e). The sideway illumination to the tissue material was ensured by an *in situ* power measurement during the probe assembly.

C. Tapered Fiber Probe
For a flat end-facet fiber even with side-firing, the light penetration depth is around a few hundred micrometers. This is mainly due to the strong absorption of the tissue. Increasing the interaction volume with biomaterials at the targeted region or illumination of spatially extended tissue regions is expected. By tapering an MMF gradually shrinks the cladding diameter from ~200 μm down to 500 nm within a few millimeters of length. The tapered fiber probe exposes a large area for light emission through ray radiation into the surrounding [152–154]. For use in optogenetic manipulation of small nuclei where larger than 100 μm fiber tips can easily damage the bio-organisms, the tapered fibers can be used to scan for multiple layers to search for a strong behavioral effect when the tissues are optogenetically activated. Some special materials such as crystalline Al_2O_3 could be used to fabricate fiber probes. New functions such as optically stimulated luminescence (OSL) could be obtained. A green laser was fed into the optical fiber and stimulated OSL from the dosimeter connected at the distal end, as shown in Ref. [155].

D. Multi-emitting Fiber Probe
In recent years, there has been an effort to increase the stimulating optrode from a single point to multiple points. With the
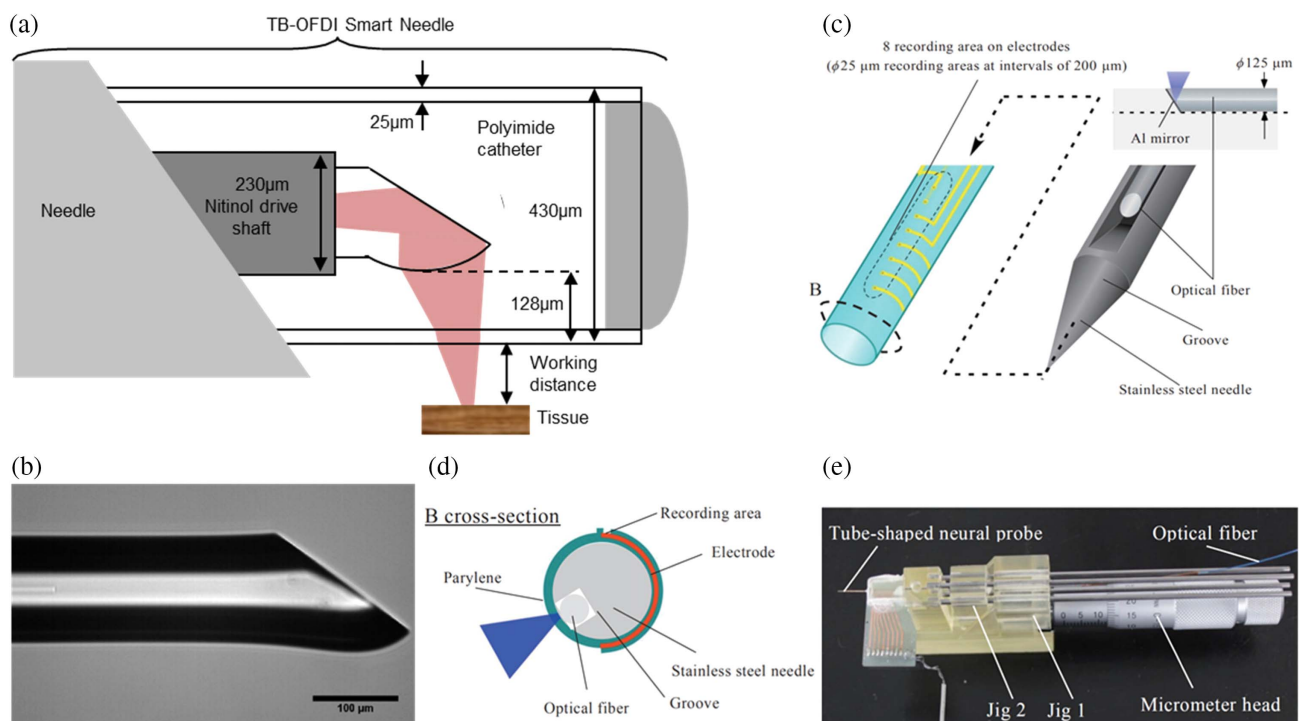

Fig. 7. Selected examples of angled and tapered fiber probes for *in vivo* applications. (a) Flexible transbronchial smart needle with angle fiber probe for biopsy guidance. (b) Microscopic photograph of the polished ball-lens optical probe. (Reprinted with permission from [150]. Copyright Optical Society of America.) (c) Schematics, (d) cross-sectional view, (e) integrated device of flexible tube-shaped neural probe for recording and optical stimulation of neurons at arbitrary depths. (Adapted with permission from [151]. Copyright Optical Society of America.)
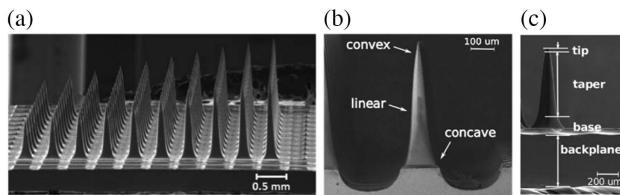
Fig. 8. Three-dimensional optrode array for infrared neural stimulation. (a) SEM micrograph of the 3D optrodes array with different lengths, (b) tapered profile of the 3D optrode tip, and (c) a detailed description of the structure. (Reprinted with permission from [157]. Copyright Optical Society of America.)

Fig. 9. Ray tracing simulation of a contact focusing three-sphere microprobe. (Reprinted with permission from [162]. Copyright Optical Society of America.)

increased density of stimulation and readout points, more information about the spatial distribution and even neuron circuitry connectivity could be obtained. The fabrication methods of the probes with multiemission functions require precision manufacturing down to the sub-micrometer level. The diameter of a standard silica fiber was tapered down from 125 μm to 200 nm at the tip by a "heating and pulling" method. Then the tapered region was coated with 300 nm gold film as reflective material to prevent leakage of light in propagation. A few local optical windows were created by removing the metallic coating using a focused Ga^+ ion beam system. The window dimensions (width and depth) were varying along the tapered region, but with a fixed adjacent distance. Both simulation and experimental results have demonstrated the capability of the fiber probe to provide multiple emitting points along a single fiber (up to seven in Ref. [156]). More interestingly, multiple wavelengths of the light beam could be independently delivered via a single fiber. This was realized by only changing the input angle of the light source to fiber coupling. A red emission beam and a green emission beam were output from two separate optical windows.

However, the above probe only demonstrated multiple emission in the vertical direction. In many other applications, multiple emission along the transverse direction is in need as well. Abaya *et al.* have fabricated a three-dimensional optrode array for infrared neural stimulation [157]. The 10 × 10 array of optrodes with rows of varying lengths from 500 μm to 1.5 mm on a 400 μm pitch was fabricated on an undoped silicon substrate, as shown in Figs. 8(a)–8(c). An optical fiber was used at the back of the tip for coupling in this case; these tips also perform the function of miniaturized optical waveguides. More comprehensive designs and integrations with commercial neural interfacing devices can be found in Ref. [158]. It is worth mentioning here that the optical sources with near-infrared wavelengths at 1.87 μm and 2.1 μm have been identified as effective stimulation sources. They have been found with practical potential since they not only provide minimal nerve damage, but also correspond to a tissue penetration depth over 300 μm.

E. Other Fiber Probe Designs

New optical approaches have in turn inspired the development of new technologies to optically interface with the central nerve systems. New classes of implantable nanophotonic and microphotonic devices have emerged for investigating causal connec-
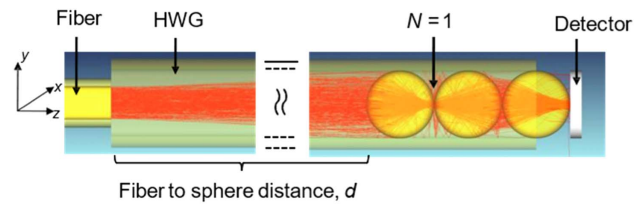
tions in brain microcircuits, employing a combination of multipoint optical control and readout of brain activities [159–161]. One example of the special probe design was shown in Fig. 9. A chain design by three or five high-index spheres was proposed on the fiber probe [162]. Numerical simulation shows a twofold improvement in spatial resolution over a single sphere design could be achieved with 20%–40% optical loss. Sophisticated probe designs such as using a microlens or axicon on fiber tip [163] could potentially achieve high precision in beam delivery, but the complexity in fabrication control may remain as a challenge.

Beam engineering is a research direction that has drawn a lot of interest. Laser beam shaping is a potential technique to optimize light–biomaterial interactions, especially in improving the uniformity of the energy distribution. Through wet chemical etching of the distal fiber tip, a concave shape was produced to help transform the Gaussian spatial beam to a top-hat beam profile, as described in Ref. [164]. The redistribution of laser energy improves the beam utilization efficiency, minimizes the local hot spot, and hence avoids tissue damage. Moreover, the flat-top beam profile provides more uniform nerve irradiation and simplifies the alignment of the laser beam.

Nonlinear effects such as two-photon fluorescence could be excited by delivery of an ultrafast femtosecond laser [165]. However, compared with setups using microscope objectives and complex scanning beam geometries, the fiber tip provides cellular circuitry probing with more precise spatial modulation. Combining microendoscopy with laser stimulation is a collaborative effort between nonlinear optical imaging and optogenetics, which is another trend for deep brain research [166]. Although most literature presented fiber probes application in brain-related optical stimulation, it can be extended to other organs as well, such as the heart [167]. Klimas *et al.* summarized a group of genetically encoded optical indicators and actuators. Light from the fiber is focused onto the sample using an endoscopic probe. The fluorescence signal is then coupled back into the fiber using the same probe and sent to the detector using a dichroic mirror. A fiber bundle-based integrated platform for wide-field bioimaging and structured/modulated optical stimulation in the deep brain is another trend for precision targeting.

After or during optical stimulation, the electrical signal was mainly collected as an observing parameter for biomedical analysis. However, the optical fiber itself can be designed based on the optical coupler/splitter concept, in order to retrieve the reflection signal. In this case, a photometry device

can be integrated with fiber stimulation [168] for an all-optical approach.

5. DISCUSSION AND CONCLUSION

In this paper, first, the resonance-based and interference-based optical fiber sensors demonstrated within the recent 5 years have been reviewed. The sensors are categorized based on different sensing principles. For each sensor type, fiber sensor probe design and measurement results have been illustrated in the figures. Also, the sensing mechanism, functional material, working wavelength, analyte type, sensitivity, and LOD have been summarized in the corresponding tables. Various functional materials including metal-organic framework and covalent organic framework have been applied to enhance the sensor performance [169–175]. It is worth noting that these materials have drawn a lot of interest in biosensing contributed by their biocompatibility [176–178]. Hence, one of the focuses for future work could be the exploration of novel functional materials for various bioanalyte samples to demonstrate the lab-on-fiber sensor devices [21,179] with high sensitivity, selectivity, and low LOD.

Regarding imaging probes, we have systematically reviewed the roles of optical fibers including as the excitation source, as the light delivering medium, and as the signal collection channel in various bioimaging applications. Fibers are flexible and excellent waveguides for endoscopy and remote imaging applications. However, the effect of bending, twist angles, and linear motion of the fiber probe on the imaging quality has to be carefully examined, which may be complex compared to conventional plane waveguides. In the future, one of the exciting areas to explore is the rapid advancement of fiber fabrication technologies and nanotechnologies; optical fibers with patterned nanostructures will be empowered with added functionalities such as beam steering [180], beam focusing [181], and Bessel beam generation [182], which can be readily applied in the biomedical imaging field. Another area of exploration is on the quantitative phase and polarization-sensitive imaging. Biological objects, such as amino acids, enzymes, glucose, and collagen, possess intrinsic polarization (or chirality or handedness). Polarization is also an indication of the health of certain tissues and cells. Hence, polarization-sensitive imaging is an important research topic in the biology community. Conventionally, it is relying on cascading of multiple optical components in a sophisticated setup that is bulky. Lin *et al.* developed an all optical fiber-based polarization-sensitive OCT imaging system where bulk quarter-wave plates were replaced by fiber optics polarization controllers. The system was demonstrated with *in vivo* imaging of human fingertip and nail [183]. Similarly, Fu *et al.* developed a fiber-optic catheter-based polarization-sensitive OCT imaging system. Experiments were conducted on biological samples such as human finger skin *in vivo*, and untreated and thermally ablated porcine myocardium *ex vivo*. The obtained phase retardation images based on the tissue birefringence and the scattered intensity information provide more accurate and robust results than conventional OCT alone [184]. Gordon *et al.* used a fiber bundle for the quantitative phase and polarization-sensitive imaging, which can be easily applied on biosamples [185]. One of the applications

of PCFs is the polarization-maintaining fibers. Future work in this area can be the design of PCFs for a shorter beat length that reduces the bend-induced coupling between polarization states and thus a high polarization extinction ratio, as well as much reduced thermal sensitivity of birefringence.

The challenges for next-generation fiber-based stimulation probes as a multifunctional device will be their compatibility with existing high-resolution or whole-brain imaging and stimulation techniques. Multimodality and integration with existing systems, for example, with magnetic resonance imaging, are shown in Refs. [159,186,187]. To link brain function to behavior, optical approaches should also be compatible with untethered and free-moving animal models. This will require the integrated remote/wireless systems to have control of multiple optical stimulations and drug delivery. Experiments in freely moving animals would also be facilitated by the development of wireless powering systems, to mitigate the weight and undependability of on-board batteries. Various components of optogenetic neural interfaces, expected multipoint optical modulation and control of neural activity, as well as *in situ* drug delivery and specific monitoring of neurotransmitter release, could be demonstrated for *in vivo* prototypes.

In summary, optical fibers could be considered as a class of flexible optical platform. They offer remote-access capabilities that could not be easily realized in free-space optical components. The microfabrication and nanofabrication technologies on the fiber and in the fiber make the diversity of new functionalities integrated in the updated generation of devices, including sensors, imaging, and stimulation probes. Looking forward, to achieve compactness enabled by microintegration technologies, light-weight as well as biocompatible materials could be the technical challenges with future potentials. From the optical engineering perspective, spatiotemporal beam shaping, ultrafast laser for nonlinear optics, and compatibility with existing biomedical approaches to realize multimodalities are the trends in fiber probes technology.

List of abbreviations

AFM	atomic force microscopy
ATP	aminothiophenol
bBSA	biotinylated bovine serum albumin
CARS	coherent anti-Stokes Raman scattering
CRP	C-reactive protein
CS	chitosan
CTAB	cetyltrimethylammonium bromide
DCPCF	double-clad photonic crystal fiber
FBG	fiber Bragg grating
FP	Fabry-Perot
GO	graphene oxide
GRIN	graded-index
HCF	hollow-core fiber
IgG	immunoglobulin G
ITO	indium tin oxide
LCPCF	liquid-core photonic crystal fiber
LGUS	laser-generated ultrasound
LMR	lossy mode resonance
LOD	limit of detection
LPFG (or LPG)	long-period fiber grating

LSPR	localized surface plasmon resonance
MMF	multimode fiber
NA	numerical aperture
NCF	noncore fiber
Ni	nickel
NIR	near-infrared
NP	nanoparticle
OCT	optical coherence tomography
OSL	optically stimulated luminescence
OTA	ochratoxin A
PAI	photoacoustic imaging
PBGF	photonic bandgap fiber
PCF	photonic crystal fiber
PD	polishing depth
PMMA	poly-methacrylate
PS	polystyrene
PVB	polyvinyl butyral
R6G	rhodamine 6G
Rh	rhodamine
RIU	refractive index unit
SA	streptavidin
SCF	solid-core fiber
SEM	scanning electron microscopy
SERS	surface-enhanced Raman scattering
SMF	single-mode fiber
SNOM	scanning near-field optical microscopy
SNP	silver nanoparticles
SPR	surface plasmon resonance
SRI	surrounding refractive index
TCMMF	tip-coated multimode fiber
TFBG	tilted fiber Bragg gratings
WD	working distance

Disclosures. The authors declare no conflicts of interest.

REFERENCES

1. C. Jauregui, J. Limpert, and A. Tünnermann, "High-power fibre lasers," Nat. Photonics **7**, 861–867 (2013).
2. N. Li, J. Xue, C. Ouyang, K. Wu, J. H. Wong, S. Aditya, and P. P. Shum, "Cavity-length optimization for high energy pulse generation in a long cavity passively mode-locked all-fiber ring laser," Appl. Opt. **51**, 3726–3730 (2012).
3. J. Xue, N. Li, K. Wu, J. H. Wong, C. Ouyang, S. Aditya, and P. P. Shum, "Performance study and assessment of phase noise suppression by incoherent addition in a mode-locked fiber laser system," Opt. Commun. **285**, 153–157 (2012).
4. S. D. Jackson, "Towards high-power mid-infrared emission from a fibre laser," Nat. Photonics **6**, 423–431 (2012).
5. Y. Liu, K. Wu, N. Li, L. Lan, S. Yoo, X. Wu, P. P. Shum, S. Zeng, and X. Tan, "Regenerative Er-doped fiber amplifier system for high-repetition-rate optical pulses," J. Opt. Soc. Korea **17**, 357–361 (2013).
6. N. Li, S. Yoo, X. Yu, D. Jain, and J. K. Sahu, "Pump power depreciation by photodarkening in ytterbium-doped fibers and amplifiers," IEEE Photonics Technol. Lett. **26**, 115–118 (2014).
7. O. Tzang, A. M. Caravaca-Aguirre, K. Wagner, and R. Piestun, "Adaptive wavefront shaping for controlling nonlinear multimode interactions in optical fibres," Nat. Photonics **12**, 368–374 (2018).
8. J. H. Wong, H. Q. Lam, S. Aditya, J. Zhou, N. Li, J. Xue, P. H. Lim, K. E. K. Lee, K. Wu, and P. P. Shum, "Photonic generation of frequency-tunable microwave signals using an array of uniformly spaced optical combs," J. Lightwave Technol. **30**, 3164–3172 (2012).
9. J. E. Betancur-Ochoa, V. P. Minkovich, and Y. J. Montagut-Ferizzola, "Special photonic crystal modal interferometer for highly sensitive biosensing," J. Lightwave Technol. **35**, 4747–4751 (2017).
10. J. B. Jensen, P. E. Hoiby, G. Emiliyanov, O. Bang, L. H. Pedersen, and A. Bjarklev, "Selective detection of antibodies in microstructured polymer optical fibers," Opt. Express **13**, 5883–5889 (2005).
11. J. Zheng, X. Tang, Z. Yang, Z. Liang, Y. Chen, K. Wang, Y. Song, Y. Zhang, J. Ji, Y. Liu, D. Fan, and H. Zhang, "Few-layer phosphorene-decorated microfiber for all-optical thresholding and optical modulation," Adv. Opt. Mater. **5**, 1700026 (2017).
12. X. Jiang, L. Zhang, S. Liu, Y. Zhang, Z. He, W. Li, F. Zhang, Y. Shi, W. Lü, Y. Li, Q. Wen, J. Li, J. Feng, S. Ruan, Y.-J. Zeng, X. Zhu, Y. Lu, and H. Zhang, "Ultrathin metal-organic framework: an emerging broadband nonlinear optical material for ultrafast photonics," Adv. Opt. Mater. **6**, 1800561 (2018).
13. F. Esposito, L. Sansone, C. Taddei, S. Campopiano, M. Giordano, and A. Iadicicco, "Ultrasensitive biosensor based on long period grating coated with polycarbonate-graphene oxide multilayer," Sens. Actuators B **274**, 517–526 (2018).
14. R. Ravikumar, L. H. Chen, P. Jayaraman, C. L. Poh, and C. C. Chan, "Chitosan-nickel film based interferometric optical fiber sensor for label-free detection of histidine tagged proteins," Biosens. Bioelectron. **99**, 578–585 (2018).
15. A. M. Zheltikov, "Microstructure fibers in biophotonics," in *Handbook of Biophotonics* (Wiley, 2013), Chap. 4.
16. H. Tu and S. A. Boppart, "Coherent fiber supercontinuum for biophotonics," Laser Photonics Rev. **7**, 628–645 (2013).
17. E. S. Boyden, "Optogenetics and the future of neuroscience," Nat. Neurosci. **18**, 1200–1201 (2015).
18. V. Gradinaru, K. R. Thompson, F. Zhang, M. Mogri, K. Kay, M. B. Schneider, and K. Deisseroth, "Targeting and readout strategies for fast optical neural control *in vitro* and *in vivo*," J. Neurosci. **27**, 14231–14238 (2007).
19. F. Chiavaioli, F. Baldini, S. Tombelli, C. Trono, and A. Giannetti, "Biosensing with optical fiber gratings," Nanophotonics **6**, 663–679 (2017).
20. C. Caucheteur, T. Guo, and J. Albert, "Review of plasmonic fiber optic biochemical sensors: improving the limit of detection," Anal. Bioanal. Chem. **407**, 3883–3897 (2015).
21. P. Vaiano, B. Carotenuto, M. Pisco, A. Ricciardi, G. Quero, M. Consales, A. Crescitelli, E. Esposito, and A. Cusano, "Lab on fiber technology for biological sensing applications," Laser Photonics Rev. **10**, 922–961 (2016).
22. A. B. Socorro-Leránoz, D. Santano, I. Del Villar, and I. R. Matias, "Trends in the design of wavelength-based optical fibre biosensors (2008–2018)," Biosens. Bioelectron.: X **1**, 100015 (2019).
23. B. A. Flusberg, E. D. Cocker, W. Piyawattanametha, J. C. Jung, E. L. M. Cheung, and M. J. Schnitzer, "Fiber-optic fluorescence imaging," Nat. Methods **2**, 941–950 (2005).
24. G. Keiser, F. Xiong, Y. Cui, and P. P. Shum, "Review of diverse optical fibers used in biomedical research and clinical practice," J. Biomed. Opt. **19**, 080902 (2014).
25. J. Li, H. Ebendorff-Heidepriem, B. C. Gibson, A. D. Greentree, M. R. Hutchinson, P. Jia, R. Kostecki, G. Liu, A. Orth, M. Ploschner, E. P. Schartner, S. C. Warren-Smith, K. Zhang, G. Tsiminis, and E. M. Goldys, "Perspective: biomedical sensing and imaging with optical fibers—Innovation through convergence of science disciplines," APL Photonics **3**, 100902 (2018).

26. J. H. Ahn, T. Y. Seong, W. M. Kim, T. S. Lee, I. Kim, and K.-S. Lee, "Fiber-optic waveguide coupled surface plasmon resonance sensor," Opt. Express **20**, 21729–21738 (2012).

27. H.-Y. Lin, Y.-C. Tsao, W.-H. Tsai, Y.-W. Yang, T.-R. Yan, and B.-C. Sheu, "Development and application of side-polished fiber immunosensor based on surface plasmon resonance for the detection of Legionella pneumophila with halogens light and 850 nm-LED," Sens. Actuators A **138**, 299–305 (2007).

28. J. Pollet, F. Delport, D. T. Thi, M. Wevers, and J. Lammertyn, "Aptamer-based surface plasmon resonance probe," in *Sensors* (IEEE, 2008), pp. 1187–1190.

29. M. Kanso, S. Cuenot, and G. Louarn, "Sensitivity of optical fiber sensor based on surface plasmon resonance: modeling and experiments," Plasmonics **3**, 49–57 (2008).

30. Y. S. Dwivedi, A. K. Sharma, and B. D. Gupta, "Influence of design parameters on the performance of a surface plasmon sensor based fiber optic sensor," Plasmonics **3**, 79–86 (2008).

31. R. Slavík, J. Homola, and E. Brynda, "A miniature fiber optic surface plasmon resonance sensor for fast detection of staphylococcal enterotoxin B," Biosens. Bioelectron. **17**, 591–595 (2002).

32. S. Cao, Y. Shao, Y. Wang, T. Wu, L. Zhang, Y. Huang, F. Zhang, C. Liao, J. He, and Y. Wang, "Highly sensitive surface plasmon resonance biosensor based on a low-index polymer optical fiber," Opt. Express **26**, 3988–3994 (2018).

33. N. M. Y. Zhang, K. Li, P. P. Shum, X. Yu, S. Zeng, Z. Wu, Q. J. Wang, K. T. Yong, and L. Wei, "Hybrid graphene/gold plasmonic fiber-optic biosensor," Adv. Mater. Technol. **2**, 1600185 (2017).

34. X. Yu, D. Yong, H. Zhang, H. Li, Y. Zhang, C. C. Chan, H.-P. Ho, H. Liu, and D. Liu, "Plasmonic enhanced fluorescence spectroscopy using side-polished microstructured optical fiber," Sens. Actuators B **160**, 196–201 (2011).

35. M.-C. Navarrete, N. Díaz-Herrera, A. González-Cano, and Ó. Esteban, "Surface plasmon resonance in the visible region in sensors based on tapered optical fibers," Sens. Actuators B **190**, 881–885 (2014).

36. Ó. Esteban, F. B. Naranjo, N. Díaz-Herrera, S. Valdueza-Felip, M.-C. Navarrete, and A. González-Cano, "High-sensitive SPR sensing with indium nitride as a dielectric overlay of optical fibers," Sens. Actuators B **158**, 372–376 (2011).

37. T. Wieduwilt, K. Kirsch, J. Dellith, R. Willsch, and H. Bartelt, "Optical fiber micro-taper with circular symmetric gold coating for sensor applications based on surface plasmon resonance," Plasmonics **8**, 545–554 (2013).

38. R. K. Verma, A. K. Sharma, and B. D. Gupta, "Surface plasmon resonance based tapered fiber optic sensor with different taper profiles," Opt. Commun. **281**, 1486–1491 (2008).

39. N. M. Y. Zhang, K. Li, T. Zhang, P. Shum, Z. Wang, Z. Wang, N. Zhang, J. Zhang, T. Wu, and L. Wei, "Electron-rich two-dimensional molybdenum trioxides for highly integrated plasmonic biosensing," ACS Photonics **5**, 347–352 (2018).

40. X. Yu, Y. Zhang, S. Pan, P. Shum, M. Yan, Y. Leviatan, and C. Li, "A selectively coated photonic crystal fiber based surface plasmon resonance sensor," J. Opt. **12**, 015005 (2009).

41. Y. Zhang, L. Xia, C. Zhou, X. Yu, H. Liu, D. Liu, and Y. Zhang, "Microstructured fiber based plasmonic index sensor with optimized accuracy and calibration relation in large dynamic range," Opt. Commun. **284**, 4161–4166 (2011).

42. Y. Zhang, C. Zhou, L. Xia, X. Yu, and D. Liu, "Wagon wheel fiber based multichannel plasmonic sensor," Opt. Express **19**, 22863–22873 (2011).

43. N. M. Y. Zhang, D. J. J. Hu, P. P. Shum, Z. Wu, K. Li, T. Huang, and L. Wei, "Design and analysis of surface plasmon resonance sensor based on high-birefringent microstructured optical fiber," J. Opt. **18**, 065005 (2016).

44. B. Lee, J.-H. Park, J.-Y. Byun, J. H. Kim, and M.-G. Kim, "An optical fiber-based LSPR aptasensor for simple and rapid *in-situ* detection of ochratoxin A," Biosens. Bioelectron. **102**, 504–509 (2018).

45. H.-H. Jeong, N. Erdene, J.-H. Park, D.-H. Jeong, H.-Y. Lee, and S.-K. Lee, "Real-time label-free immunoassay of interferon-gamma and prostate-specific antigen using a fiber-optic localized surface plasmon resonance sensor," Biosens. Bioelectron. **39**, 346–351 (2013).

46. H.-H. Jeong, S.-K. Lee, J.-H. Park, N. Erdene, and D.-H. Jeong, "Fabrication of fiber-optic localized surface plasmon resonance sensor and its application to detect antibody-antigen reaction of interferon-gamma," Opt. Eng. **50**, 124405 (2011).

47. S.-W. Lee, K.-S. Lee, J. Ahn, J.-J. Lee, M.-G. Kim, and Y.-B. Shin, "Highly sensitive biosensing using arrays of plasmonic Au nanodisks realized by nanoimprint lithography," ACS Nano **5**, 897–904 (2011).

48. M. Sanders, Y. Lin, J. Wei, T. Bono, and R. G. Lindquist, "An enhanced LSPR fiber-optic nanoprobe for ultrasensitive detection of protein biomarkers," Biosens. Bioelectron. **61**, 95–101 (2014).

49. S. Kumar, B. K. Kaushik, R. Singh, N.-K. Chen, Q. S. Yang, X. Zhang, W. Wang, and B. Zhang, "LSPR-based cholesterol biosensor using a tapered optical fiber structure," Biomed. Opt. Express **10**, 2150–2160 (2019).

50. N. M. Y. Zhang, M. Qi, Z. Wang, Z. Wang, M. Chen, K. Li, P. Shum, and L. Wei, "One-step synthesis of cyclodextrin-capped gold nanoparticles for ultra-sensitive and highly-integrated plasmonic biosensors," Sens. Actuators B **286**, 429–436 (2019).

51. M. Marciniak, J. Grzegorzewski, and M. Szustakowski, "Analysis of lossy mode cut-off conditions in planar waveguides with semiconductor guiding layer," IEE Proc. J. Optoelectronics **140**, 247–252 (1993).

52. F. Chiavaioli, P. Zubiate, I. Del Villar, C. R. Zamarreño, A. Giannetti, S. Tombelli, C. Trono, F. J. Arregui, I. R. Matias, and F. Baldini, "Femtomolar detection by nanocoated fiber label-free biosensors," ACS Sens. **3**, 936–943 (2018).

53. Q. Wang and B.-T. Wang, "Surface plasmon resonance biosensor based on graphene oxide/silver coated polymer cladding silica fiber," Sens. Actuators B **275**, 332–338 (2018).

54. P. Zubiate, C. R. Zamarreño, P. Sánchez, I. R. Matias, and F. J. Arregui, "High sensitive and selective C-reactive protein detection by means of lossy mode resonance based optical fiber devices," Biosens. Bioelectron. **93**, 176–181 (2017).

55. U. S. Dinish, F. Beffara, G. Humbert, J.-L. Auguste, and M. Olivo, "Surface-enhanced Raman scattering-active photonic crystal fiber probe: towards next generation liquid biopsy sensor with ultra high sensitivity," J. Biophotonics **12**, e201900027 (2019).

56. H. Ko, S. Singamaneni, and V. V. Tsukruk, "Nanostructured surfaces and assemblies as SERS media," Small **4**, 1576–1599 (2008).

57. M. Moskovits, "Surface-enhanced Raman spectroscopy: a brief retrospective," J. Raman Spectrosc. **36**, 485–496 (2005).

58. J. P. Camden, J. A. Dieringer, J. Zhao, and R. P. Van Duyne, "Controlled plasmonic nanostructures for surface-enhanced spectroscopy and sensing," Acc. Chem. Res. **41**, 1653–1661 (2008).

59. T. Gong, Y. Cui, D. Goh, K. K. Voon, P. P. Shum, G. Humbert, J.-L. Auguste, X.-Q. Dinh, K.-T. Yong, and M. Olivo, "Highly sensitive SERS detection and quantification of sialic acid on single cell using photonic-crystal fiber with gold nanoparticles," Biosens. Bioelectron. **64**, 227–233 (2015).

60. U. S. Dinish, C. Y. Fu, K. S. Soh, B. Ramaswamy, A. Kumar, and M. Olivo, "Highly sensitive SERS detection of cancer proteins in low sample volume using hollow core photonic crystal fiber," Biosens. Bioelectron. **33**, 293–298 (2012).

61. A. Khetani, J. Riordon, V. Tiwari, A. Momenpour, M. Godin, and H. Anis, "Hollow core photonic crystal fiber as a reusable Raman biosensor," Opt. Express **21**, 12340–12350 (2013).

62. A. Khetani, A. Momenpour, E. I. Alarcon, and H. Anis, "Hollow core photonic crystal fiber for monitoring leukemia cells using surface enhanced Raman scattering (SERS)," Biomed. Opt. Express **6**, 4599–4609 (2015).

63. Y. Han, S. Tan, M. K. K. Oo, D. Pristinski, S. Sukhishvili, and H. Du, "Towards full-length accumulative surface-enhanced Raman scattering-active photonic crystal fibers," Adv. Mater. **22**, 2647–2651 (2010).

64. C. Liu, S. Wang, G. Chen, S. Xu, Q. Jia, J. Zhou, and W. Xu, "A surface-enhanced Raman scattering (SERS)-active optical fiber sensor based on a three-dimensional sensing layer," Sens. Bio-Sens. Res. **1**, 8–14 (2014).

65. X. Yang, C. Gu, F. Qian, Y. Li, and J. Z. Zhang, "Highly sensitive detection of proteins and bacteria in aqueous solution using surface-enhanced Raman scattering and optical fibers," Anal. Chem. **83**, 5888–5894 (2011).

66. F. Eftekhari, A. Lee, E. Kumacheva, and A. S. Helmy, "Examining metal nanoparticle surface chemistry using hollow-core, photonic-crystal, fiber-assisted SERS," Opt. Lett. **37**, 680–682 (2012).

67. V. S. Tiwari, A. Khetani, A. Momenpour, and H. Anis, "Optimum size and volume of nanoparticles within hollow core photonic crystal fiber," IEEE J. Sel. Top. Quantum Electron. **20**, 205–212 (2014).

68. N. Zhang, G. Humbert, T. Gong, P. P. Shum, K. Li, J.-L. Auguste, Z. Wu, D. J. J. Hu, F. Luan, Q. X. Dinh, M. Olivo, and L. Wei, "Side-channel photonic crystal fiber for surface enhanced Raman scattering sensing," Sens. Actuators, B **223**, 195–201 (2016).

69. T. Gong, N. Zhang, K. V. Kong, D. Goh, C. Ying, J.-L. Auguste, P. P. Shum, L. Wei, G. Humbert, K.-T. Yong, and M. Olivo, "Rapid SERS monitoring of lipid-peroxidation-derived protein modifications in cells using photonic crystal fiber sensor," J. Biophotonics **9**, 32–37 (2016).

70. T. B. Pham, T. H. C. Hoang, V. H. Pham, V. C. Nguyen, T. V. Nguyen, D. C. Vu, V. H. Pham, and H. Bui, "Detection of Permethrin pesticide using silver nano-dendrites SERS on optical fibre fabricated by laser-assisted photochemical method," Sci. Rep. **9**, 12590 (2019).

71. J. Cao, D. Zhao, and Q. Mao, "A highly reproducible and sensitive fiber SERS probe fabricated by direct synthesis of closely packed AgNPs on the silanized fiber taper," Analyst **142**, 596–602 (2017).

72. L. Li, S. Deng, H. Wang, R. Zhang, K. Zhu, Y. Lu, Z. Wang, S. Zong, Z. Wang, and Y. Cui, "A SERS fiber probe fabricated by layer-by-layer assembly of silver sphere nanoparticles and nanorods with a greatly enhanced sensitivity for remote sensing," Nanotechnology **30**, 255503 (2019).

73. J. Guo, Y. Luo, C. Yang, and L. Kong, "*In situ* surface-enhanced Raman scattering sensing with soft and flexible polymer optical fiber probes," Opt. Lett. **43**, 5443–5446 (2018).

74. H. Zhou, J. Liu, H. Liu, and Z. Zheng, "Compact dual-fiber surface-enhanced Raman scattering sensor with monolayer gold nanoparticles self-assembled on optical fiber," Appl. Opt. **57**, 7931–7937 (2018).

75. C. Shi, C. Lu, C. Gu, L. Tian, R. Newhouse, S. Chen, and J. Z. Zhang, "Inner wall coated hollow core waveguide sensor based on double substrate surface enhanced Raman scattering," Appl. Phys. Lett. **93**, 153101 (2008).

76. P. Pinkhasova, H. Chen, J. Kanka, P. Mergo, and H. Du, "Nanotag-enabled photonic crystal fiber as quantitative surface-enhanced Raman scattering optofluidic platform," Appl. Phys. Lett. **106**, 071106 (2015).

77. H. Yan, J. Liu, C. Yang, G. Jin, C. Gu, and L. Hou, "Novel index-guided photonic crystal fiber surface-enhanced Raman scattering probe," Opt. Express **16**, 8300–8305 (2008).

78. A. Amezcua-Correa, J. Yang, C. E. Finlayson, A. C. Peacock, J. R. Hayes, P. J. A. Sazio, J. J. Baumberg, and S. M. Howdle, "Surface-enhanced Raman scattering using microstructured optical fiber substrates," Adv. Funct. Mater. **17**, 2024–2030 (2007).

79. Y. Zhang, D. Yong, X. Yu, L. Xia, D. Liu, and Y. Zhang, "Amplification of surface-enhanced Raman scattering in photonic crystal fiber using offset launch method," Plasmonics **8**, 209–215 (2013).

80. X. Yang, C. Shi, D. Wheeler, R. Newhouse, B. Chen, J. Z. Zhang, and C. Gu, "High-sensitivity molecular sensing using hollow-core photonic crystal fiber and surface-enhanced Raman scattering," J. Opt. Soc. Am. A **27**, 977–984 (2010).

81. L. Sirleto, A. Vergara, and M. A. Ferrara, "Advances in stimulated Raman scattering in nanostructures," Adv. Opt. Photonics **9**, 169–217 (2017).

82. S. Gottardo, R. Sapienza, P. D. García, A. Blanco, D. S. Wiersma, and C. López, "Resonance-driven random lasing," Nat. Photonics **2**, 429–432 (2008).

83. W. H. Bragg and W. L. Bragg, "The reflection of X-rays by crystals," Proc. R. Soc. London Ser. A **88**, 428–438 (1913).

84. S. Sridevi, K. S. Vasu, S. Asokan, and A. K. Sood, "Sensitive detection of C-reactive protein using optical fiber Bragg gratings," Biosens. Bioelectron. **65**, 251–256 (2015).

85. J. Albert, L.-Y. Shao, and C. Caucheteur, "Tilted fiber Bragg grating sensors," Laser Photonics Rev. **7**, 83–108 (2013).

86. P. Biswas, F. Chiavaioli, S. Jana, N. Basumallick, C. Trono, A. Giannetti, S. Tombelli, A. Mallick, F. Baldini, and S. Bandyopadhyay, "Design, fabrication and characterisation of silica-titania thin film coated over coupled long period fibre gratings: towards bio-sensing applications," Sens. Actuators B **253**, 418–427 (2017).

87. X. Yu, P. Shum, and G. B. Ren, "Highly sensitive photonic crystal fiber-based refractive index sensing using mechanical long-period grating," IEEE Photonics Technol. Lett. **20**, 1688–1690 (2008).

88. N. M. Y. Zhang, X. Dong, P. P. Shum, D. J. J. Hu, H. Su, W. S. Lew, and L. Wei, "Magnetic field sensor based on magnetic-fluid-coated long-period fiber grating," J. Opt. **17**, 065402 (2015).

89. J. Li, H. Qu, and M. Skorobogatiy, "Squeezed hollow-core photonic Bragg fiber for surface sensing applications," Opt. Express **24**, 15687–15701 (2016).

90. J. Li and K. Nallappan, "Optimization of hollow-core photonic Bragg fibers towards practical sensing implementations," Opt. Mater. Express **9**, 1640–1653 (2019).

91. D. Yong, X. Yu, G. Ren, H. Zhang, Y. Zhang, C. C. Chan, H. Wei, and W. Tong, "Photonic bandgap fiber for infiltration-free refractive-index sensing," IEEE J. Sel. Top. Quantum Electron. **18**, 1560–1565 (2012).

92. Y. Cardona-Maya, A. B. Socorro, I. Del Villar, J. L. Cruz, J. M. Corres, and J. F. Botero-Cadavid, "Label-free wavelength and phase detection based SMS fiber immunosensors optimized with cladding etching," Sens. Actuators B **265**, 10–19 (2018).

93. A. B. Socorro, I. Del Villar, J. M. Corres, F. J. Arregui, and I. R. Matias, "Sensitivity enhancement in a multimode interference-based SMS fibre structure coated with a thin-film: theoretical and experimental study," Sens. Actuators B **190**, 363–369 (2014).

94. Y. Cardona-Maya, I. Del Villar, A. B. Socorro, J. M. Corres, I. R. Matias, and J. F. Botero-Cadavid, "Wavelength and phase detection based SMS fiber sensors optimized with etching and nanodeposition," J. Lightwave Technol. **35**, 3743–3749 (2017).

95. Q. Wu, Y. Semenova, P. Wang, and G. Farrell, "High sensitivity SMS fiber structure based refractometer–analysis and experiment," Opt. Express **19**, 7937–7944 (2011).

96. B.-T. Wang and Q. Wang, "An interferometric optical fiber biosensor with high sensitivity for IgG/anti-IgG immunosensing," Opt. Commun. **426**, 388–394 (2018).

97. D. Luna-Moreno, D. Monzón-Hernández, J. Villatoro, and G. Badenes, "Optical fiber hydrogen sensor based on core diameter mismatch and annealed Pd-Au thin films," Sens. Actuators B **125**, 66–71 (2007).

98. D. Sun, Y. Ran, and G. Wang, "Label-free detection of cancer biomarkers using an in-line taper fiber-optic interferometer and a fiber Bragg grating," Sensors **17**, 2559 (2017).

99. T. K. Yadav, R. Narayanaswamy, M. H. Abu Bakar, Y. M. Kamil, and M. A. Mahdi, "Single mode tapered fiber-optic interferometer based refractive index sensor and its application to protein sensing," Opt. Express **22**, 22802–22807 (2014).

100. R. Srinivasan, S. Umesh, S. Murali, S. Asokan, and S. S. Gorthi, "Bare fiber Bragg grating immunosensor for real-time detection of *Escherichia coli* bacteria," J. Biophotonics **10**, 224–230 (2017).

101. Y. Zhang, F. Wang, S. Qian, Z. Liu, Q. Wang, Y. Gu, Z. Wu, Z. Jing, C. Sun, and W. Peng, "A novel fiber optic surface plasmon resonance biosensors with special boronic acid derivative to detect glycoprotein," Sensors **17**, 2259 (2017).

102. C. Ribaut, M. Loyez, J.-C. Larrieu, S. Chevineau, P. Lambert, M. Remmelink, R. Wattiez, and C. Caucheteur, "Cancer biomarker sensing using packaged plasmonic optical fiber gratings: towards *in vivo* diagnosis," Biosens. Bioelectron. **92**, 449–456 (2017).

103. J.-H. Chen, J.-R. Zhao, X.-G. Huang, and Z.-J. Huang, "Extrinsic fiber-optic Fabry–Perot interferometer sensor for refractive index measurement of optical glass," Appl. Opt. **49**, 5592–5596 (2010).

104. S. Novais, M. S. Ferreira, and J. L. Pinto, "Optical fiber Fabry-Perot tip sensor for detection of water-glycerin mixtures," J. Lightwave Technol. **36**, 1576–1582 (2018).

105. M. F. Domingues, C. A. Rodriguez, J. Martins, C. Tavares, C. Marques, N. Alberto, P. André, and P. Antunes, "Cost-effective op-

tical fiber pressure sensor based on intrinsic Fabry-Perot interferometric micro-cavities," Opt. Fiber Technol. **42**, 56–62 (2018).

106. L. H. Chen, X. M. Ang, C. C. Chan, M. Shaillender, B. Neu, W. C. Wong, P. Zu, and K. C. Leong, "Layer-by-layer (chitosan/polystyrene sulfonate) membrane-based Fabry-Perot interferometric fiber optic biosensor," IEEE J. Sel. Top. Quantum Electron. **18**, 1457–1464 (2012).

107. J. Wallner, G. Lhota, D. Jeschek, A. Mader, and K. Vorauer-Uhl, "Application of bio-layer interferometry for the analysis of protein/liposome interactions," J. Pharm. Biomed. Anal. **72**, 150–154 (2013).

108. L. V. Doronina-Amitonova, I. V. Fedotov, O. I. Ivashkina, M. A. Zots, A. B. Fedotov, K. V. Anokhin, and A. M. Zheltikov, "Fiber-optic probes for in vivo depth-resolved neuron-activity mapping," J. Biophotonics **3**, 660–669 (2010).

109. S. Ishida, N. Nishizawa, T. Ohta, and K. Itoh, "Ultrahigh-resolution optical coherence tomography in 1.7 μm region with fiber laser supercontinuum in low-water-absorption samples," Appl. Phys. Express **4**, 052501 (2011).

110. S. Y. Ryu, H. Y. Choi, J. Na, W. J. Choi, and B. H. Lee, "Lensed fiber probes designed as an alternative to bulk probes in optical coherence tomography," Appl. Opt. **47**, 1510–1516 (2008).

111. M. Zhao, Y. Huang, and J. U. Kang, "Sapphire ball lens-based fiber probe for common-path optical coherence tomography and its applications in corneal and retinal imaging," Opt. Lett. **37**, 4835–4837 (2012).

112. H. Pahlevaninezhad, M. Khorasaninejad, Y.-W. W. Huang, Z. Shi, L. P. Hariri, D. C. Adams, V. Ding, A. Zhu, C.-W. W. Qiu, F. Capasso, and M. J. Suter, "Nano-optic endoscope for high-resolution optical coherence tomography in vivo," Nat. Photonics **12**, 540–547 (2018).

113. N. Yu, P. Genevet, M. A. Kats, F. Aieta, J.-P. Tetienne, F. Capasso, and Z. Gaburro, "Light propagation with phase discontinuities: generalized laws of reflection and refraction," Science **334**, 333–337 (2011).

114. L. Fu, A. Jain, H. Xie, C. Cranfield, and M. Gu, "Nonlinear optical endoscopy based on a double-clad photonic crystal fiber and a MEMS mirror," Opt. Express **14**, 1027–1032 (2006).

115. L. Fu, A. Jain, C. Cranfield, H. Xie, and M. Gu, "Three-dimensional nonlinear optical endoscopy," J. Biomed. Opt. **12**, 040501 (2007).

116. M. Balu, G. Liu, Z. Chen, B. J. Tromberg, and E. O. Potma, "Fiber delivered probe for efficient CARS imaging of tissues," Opt. Express **18**, 2380–2388 (2010).

117. W. Jung, S. Tang, T. Xie, D. T. McCormick, Y.-C. Ahn, J. Su, I. V. Tomov, T. B. Krasieva, B. J. Tromberg, and Z. Chen, "Miniaturized probe using 2 axis MEMS scanner for endoscopic multiphoton excitation microscopy," Proc. SPIE **6851**, 68510D (2008).

118. R. Le Harzic, I. Riemann, M. Weinigel, K. König, and B. Messerschmidt, "Rigid and high-numerical-aperture two-photon fluorescence endoscope," Appl. Opt. **48**, 3396–3400 (2009).

119. M. T. Myaing, J. Y. Ye, T. B. Norris, T. Thomas, J. R. Baker, Jr., W. J. Wadsworth, G. Bouwmans, J. C. Knight, and P. S. J. Russell, "Enhanced two-photon biosensing with double-clad photonic crystal fibers," Opt. Lett. **28**, 1224–1226 (2003).

120. I. V. Fedotov, A. B. Fedotov, L. V. Doronina, and A. M. Zheltikov, "Enhancement of guided-wave two-photon-excited luminescence response with a photonic-crystal fiber," Appl. Opt. **48**, 5274–5279 (2009).

121. V. P. Mitrokhin, A. B. Fedotov, A. A. Ivanov, M. V. Alfimov, and A. M. Zheltikov, "Coherent anti-Stokes Raman scattering microspectroscopy of silicon components with a photonic-crystal fiber frequency shifter," Opt. Lett. **32**, 3471–3473 (2007).

122. A. D. Savvin, A. A. Lanin, A. A. Voronin, A. B. Fedotov, and A. M. Zheltikov, "Coherent anti-Stokes Raman metrology of phonons powered by photonic-crystal fibers," Opt. Lett. **35**, 919–921 (2010).

123. J. S. Paiva, P. A. S. Jorge, C. C. Rosa, and J. P. S. Cunha, "Optical fiber tips for biological applications: from light confinement, biosensing to bioparticles manipulation," Biochim. Biophys. Acta **1862**, 1209–1246 (2018).

124. G. Longo, M. Girasole, G. Pompeo, R. Generosi, M. Luce, and A. Cricenti, "A multipurpose hybrid conventional/scanning near-field optical microscope for applications in materials science and biology," Meas. Sci. Technol. **21**, 045502 (2010).

125. V. Dalal, M. Bhattacharya, D. Narang, P. K. Sharma, and S. Mukhopadhyay, "Nanoscale fluorescence imaging of single amyloid fibrils," J. Phys. Chem. Lett. **3**, 1783–1787 (2012).

126. Y. Li, X. Liu, and B. Li, "Single-cell biomagnifier for optical nanoscopes and nanotweezers," Light Sci. Appl. **8**, 61 (2019).

127. S.-L. Chen, "Review of laser-generated ultrasound transmitters and their applications to all-optical ultrasound transducers and imaging," Appl. Sci. **7**, 25 (2016).

128. Y. Tian, N. Wu, X. Zou, H. Felemban, C. Cao, and X. Wang, "Fiber-optic ultrasound generator using periodic gold nanopores fabricated by a focused ion beam," Opt. Eng. **52**, 065005 (2013).

129. R. J. Colchester, C. A. Mosse, D. S. Bhachu, J. C. Bear, C. J. Carmalt, I. P. Parkin, B. E. Treeby, I. Papakonstantinou, and A. E. Desjardins, "Laser-generated ultrasound with optical fibres using functionalised carbon nanotube composite coatings," Appl. Phys. Lett. **104**, 173502 (2014).

130. M. C. Finlay, C. A. Mosse, R. J. Colchester, S. Noimark, E. Z. Zhang, S. Ourselin, P. C. Beard, R. J. Schillin, I. P. Parkin, I. Papakonstantinou, and A. E. Desjardins, "Through-needle all-optical ultrasound imaging in vivo: a preclinical swine study," Light Sci. Appl. **6**, e17103 (2017).

131. E. Z. Zhang and P. C. Beard, "A miniature all-optical photoacoustic imaging probe," Proc. SPIE **7899**, 78991F (2011).

132. N. E. Fisher, D. J. Webb, C. N. Pannell, D. A. Jackson, L. R. Gavrilov, J. W. Hand, L. Zhang, and I. Bennion, "Medical ultrasound detection using fiber Bragg gratings," Proc. SPIE **3541**, 27–32 (1999).

133. J. A. Guggenheim, J. Li, T. J. Allen, R. J. Colchester, S. Noimark, O. Ogunlade, I. P. Parkin, I. Papakonstantinou, A. E. Desjardins, E. Z. Zhang, and P. C. Beard, "Ultrasensitive plano-concave optical microresonators for ultrasound sensing," Nat. Photonics **11**, 714–719 (2017).

134. R. J. Colchester, E. Z. Zhang, C. A. Mosse, P. C. Beard, I. Papakonstantinou, and A. E. Desjardins, "Broadband miniature optical ultrasound probe for high resolution vascular tissue imaging," Biomed. Opt. Express **6**, 1502–1511 (2015).

135. E. Biagi, S. Cerbai, L. Masotti, A. Belsito, A. Roncaglia, G. Masetti, and N. Speciale, "Fiber optic broadband ultrasonic probe for virtual biopsy: technological solutions," in *IEEE International Ultrasonics Symposium* (IEEE, 2009), pp. 200–203.

136. Y. Miida and Y. Matsuura, "All-optical photoacoustic imaging system using fiber ultrasound probe and hollow optical fiber bundle," Opt. Express **21**, 22023–22033 (2013).

137. G. Balasundaram, L. Ding, X. Li, A. B. E. Attia, X. L. Dean-Ben, C. J. H. Ho, P. Chandrasekharan, H. C. Tay, H. Q. Lim, C. B. Ong, R. P. Mason, D. Razansky, and M. Olivo, "Noninvasive anatomical and functional imaging of orthotopic glioblastoma development and therapy using multispectral optoacoustic tomography," Transl. Oncol. **11**, 1251–1258 (2018).

138. R. Bi, G. Balasundaram, S. Jeon, H. C. Tay, Y. Pu, X. Li, M. Moothanchery, C. Kim, and M. Olivo, "Photoacoustic microscopy for evaluating combretastatin A4 phosphate induced vascular disruption in orthotopic glioma," J. Biophotonics **11**, e201700327 (2018).

139. G. Diot, S. Metz, A. Noske, E. Liapis, B. Schroeder, S. V. Ovsepian, R. Meier, E. Rummeny, and V. Ntziachristos, "Multispectral optoacoustic tomography (MSOT) of human breast cancer," Clin. Cancer Res. **23**, 6912–6922 (2017).

140. Y. Goh, G. Balasundaram, M. Moothanchery, A. Attia, X. Li, H. Q. Lim, N. Burton, Y. Qiu, T. C. Putti, C. W. Chan, P. Iau, S. W. Tang, C. W. Q. Ng, F. J. Pool, P. Pillay, W. Chua, E. Sterling, S. T. Quek, and M. Olivo, "Multispectral optoacoustic tomography in assessment of breast tumor margins during breast-conserving surgery: a first-in-human case study," Clin. Breast Cancer **18**, e1247–e1250 (2018).

141. A. B. E. Attia, S. Y. Chuah, D. Razansky, C. J. H. Ho, P. Malempati, U. S. Dinish, R. Bi, C. Y. Fu, S. J. Ford, J. S.-S. Lee, M. W. P. Tan, M. Olivo, and S. T. G. Thng, "Noninvasive real-time characterization of non-melanoma skin cancers with handheld optoacoustic probes," Photoacoustics **7**, 20–26 (2017).

142. J. Aguirre, M. Schwarz, N. Garzorz, M. Omar, A. Buehler, K. Eyerich, and V. Ntziachristos, "Precision assessment of label-free psoriasis biomarkers with ultra-broadband optoacoustic mesoscopy," Nat. Biomed. Eng. **1**, 0068 (2017).

143. D. R. Sparta, A. M. Stamatakis, J. L. Phillips, N. Hovelsø, R. van Zessen, and G. D. Stuber, "Construction of implantable optical fibers for long-term optogenetic manipulation of neural circuits," Nat. Protoc. **7**, 12–23 (2012).

144. Y.-K. Song, W. R. Patterson, C. W. Bull, J. Zhang, C. R. Sheldon, A. V. Nurmikko, J. J. Stein, M. D. Serruya, and J. P. Donoghue, "Fiber optic guided functional electrical stimulation with micro-scale photovoltaic neurostimulator devices," in *Conference on Lasers and Electro-Optics* (Optical Society of America, 2007), paper CTuEE4.

145. B. Lee, J. Jin, J. Park, and J. Kim, "Flexible neural probe integrated microchannel and optical fiber for multifle stimulation," in *Transducers & Eurosensors XXVII: The 17th International Conference on Solid-State Sensors, Actuators and Microsystems (TRANSDUCERS & EUROSENSORS XXVII)* (2013), pp. 321–324.

146. A. Canales, X. Jia, U. P. Froriep, R. A. Koppes, C. M. Tringides, J. Selvidge, C. Lu, C. Hou, L. Wei, Y. Fink, and P. Anikeeva, "Multifunctional fibers for simultaneous optical, electrical and chemical interrogation of neural circuits *in vivo*," Nat. Biotechnol. **33**, 277–284 (2015).

147. Y. Shin, M. Yoo, H.-S. Kim, S.-K. Nam, H.-I. Kim, S.-K. Lee, S. Kim, and H.-S. Kwon, "Characterization of fiber-optic light delivery and light-induced temperature changes in a rodent brain for precise optogenetic neuromodulation," Biomed. Opt. Express **7**, 4450–4471 (2016).

148. X. Tan, S. Rajguru, H. Young, N. Xia, S. R. Stock, X. Xiao, and C.-P. Richter, "Radiant energy required for infrared neural stimulation," Sci. Rep. **5**, 13273 (2015).

149. R. Pashaie and R. Falk, "Single optical fiber probe for fluorescence detection and optogenetic stimulation," IEEE Trans. Biomed. Eng. **60**, 268–280 (2013).

150. K. M. Tan, M. Shishkov, A. Chee, M. B. Applegate, B. E. Bouma, and M. J. Suter, "Flexible transbronchial optical frequency domain imaging smart needle for biopsy guidance," Biomed. Opt. Express **3**, 1947–1954 (2012).

151. S. Tamaki, T. Kuki, T. Matsunaga, H. Mushiake, Y. Furusawa, and Y. Haga, "Flexible tube-shaped neural probe for recording and optical stimulation of neurons at arbitrary depths," Sens. Mater. **27**, 507–523 (2015).

152. F. Pisanello, G. Mandelbaum, M. Pisanello, I. A. Oldenburg, L. Sileo, J. E. Markowitz, R. E. Peterson, A. Della Patria, T. M. Haynes, M. S. Emara, B. Spagnolo, S. R. Datta, M. De Vittorio, and B. L. Sabatini, "Dynamic illumination of spatially restricted or large brain volumes via a single tapered optical fiber," Nat. Neurosci. **20**, 1180–1188 (2017).

153. M. Pisanello, F. Pisano, L. Sileo, E. Maglie, E. Bellistri, B. Spagnolo, G. Mandelbaum, B. L. Sabatini, M. De Vittorio, and F. Pisanello, "Exploiting modal demultiplexing properties of tapered optical fibers for tailored optogenetic stimulation," bioRxiv 199273 (2017).

154. N. Vogt, "Tailoring optogenetic illumination through tapered fibers," Nat. Methods **14**, 763 (2017).

155. M. S. Akselrod, L. Bøtter-Jensen, and S. W. S. McKeever, "Optically stimulated luminescence and its use in medical dosimetry," Radiat. Meas. **41**, S78–S99 (2006).

156. F. Pisanello, L. Sileo, I. A. Oldenburg, M. Pisanello, L. Martiradonna, J. A. Assad, B. L. Sabatini, and M. De Vittorio, "Multipoint-emitting optical fibers for spatially addressable in vivo optogenetics," Neuron **82**, 1245–1254 (2014).

157. T. V. F. Abaya, M. Diwekar, S. Blair, P. Tathireddy, L. Rieth, G. A. Clark, and F. Solzbacher, "Characterization of a 3D optrode array for infrared neural stimulation," Biomed. Opt. Express **3**, 2200–2219 (2012).

158. F. Wu, "Implantable neural probes for electrical recording and optical stimulation of cellular level neural circuitry in behaving animals," Ph.D. thesis (University of Michigan, 2015).

159. A. Torricelli, D. Contini, A. Dalla Mora, A. Pifferi, R. Re, L. Zucchelli, M. Caffini, A. Farina, and L. Spinelli, "Neurophotonics: non-invasive optical techniques for monitoring brain functions," Funct. Neurol. **29**, 223–230 (2014).

160. Y. K. Cho, G. Zheng, G. J. Augustine, D. Hochbaum, A. Cohen, T. Knöpfel, F. Pisanello, F. S. Pavone, I. M. Vellekoop, M. J. Booth, S. Hu, J. Zhu, Z. Chen, and Y. Hoshi, "Roadmap on neurophotonics," J. Opt. **18**, 093007 (2016).

161. M. R. Warden, J. A. Cardin, and K. Deisseroth, "Optical neural interfaces," Annu. Rev. Biomed. Eng. **16**, 103–129 (2014).

162. A. Darafsheh, A. Fardad, N. M. Fried, A. N. Antoszyk, H. S. Ying, and V. N. Astratov, "Contact focusing multimodal microprobes for ultra-precise laser tissue surgery," Opt. Express **19**, 3440–3448 (2011).

163. S. K. Mohanty, K. S. Mohanty, and M. W. Berns, "Manipulation of mammalian cells using a single-fiber optical microbeam," J. Biomed. Opt. **13**, 054049 (2008).

164. S. Tozburun, "Optical stimulation of the prostate nerves: a potential diagnostic technique," Ph.D. thesis (The University of North Carolina at Charlotte, 2012).

165. K. Dhakal, L. Gu, B. Black, and S. K. Mohanty, "Fiber-optic two-photon optogenetic stimulation," Opt. Lett. **38**, 1927–1929 (2013).

166. M. Kim, J. Hong, J. Kim, and H. Shin, "Fiber bundle-based integrated platform for wide-field fluorescence imaging and patterned optical stimulation for modulation of vasoconstriction in the deep brain of a living animal," Biomed. Opt. Express **8**, 2781–2795 (2017).

167. A. Klimas and E. Entcheva, "Toward microendoscopy-inspired cardiac optogenetics in vivo: technical overview and perspective," J. Biomed. Opt. **19**, 080701 (2014).

168. I. Nishidate, C. Mizushima, K. Yoshida, S. Kawauchi, S. Sato, and M. Sato, "*In vivo* estimation of light scattering and absorption properties of rat brain using a single-reflectance fiber probe during cortical spreading depression," J. Biomed. Opt. **20**, 027003 (2015).

169. B. Chocarro-Ruiz, J. Pérez-Carvajal, C. Avci, O. Calvo-Lozano, M. I. Alonso, D. Maspoch, and L. M. Lechuga, "A CO_2 optical sensor based on self-assembled metal-organic framework nanoparticles," J. Mater. Chem. A **6**, 13171–13177 (2018).

170. H. Yuan, J. Tao, N. Li, A. Karmakar, C. Tang, H. Cai, S. J. Pennycook, N. Singh, and D. Zhao, "On-chip tailorability of capacitive gas sensors integrated with metal–organic framework films," Angew. Chem. Int. Ed. **58**, 14089–14094 (2019).

171. J. Wu, M. Yin, K. Seefeldt, A. Dani, R. Guterman, J. Yuan, A. P. Zhang, and H.-Y. Tam, "*In situ* μ-printed optical fiber-tip CO_2 sensor using a photocrosslinkable poly(ionic liquid)," Sens. Actuators B **259**, 833–839 (2018).

172. H. Yuan, N. Li, J. Linghu, J. Dong, Y. Wang, A. Karmakar, J. Yuan, M. Li, P. J. S. Buenconsejo, G. Liu, H. Cai, S. J. Pennycook, N. Singh, and D. Zhao, "Chip-level integration of covalent organic frameworks for trace benzene sensing," ACS Sens. **5**, 1474–1481 (2020).

173. S. Kanaparthi and S. G. Singh, "Chemiresistive sensor based on zinc oxide nanoflakes for CO_2 detection," ACS Appl. Nano Mater. **2**, 700–706 (2019).

174. M. R. Tchalala, Y. Belmabkhout, K. Adil, K. N. Chappanda, A. Cadiau, P. M. Bhatt, K. N. Salama, and M. Eddaoudi, "Concurrent sensing of CO_2 and H_2O from air using ultramicroporous fluorinated metal-organic frameworks: effect of transduction mechanism on the sensing performance," ACS Appl. Mater. Interfaces **11**, 1706–1712 (2019).

175. N. Li, H. Yuan, L. Xu, J. Tao, D. K. T. Ng, L. Y. T. Lee, D. D. Cheam, Y. Zeng, B. Qiang, Q. Wang, H. Cai, N. Singh, and D. Zhao, "Radiation enhancement by graphene oxide on microelectromechanical system emitters for highly selective gas sensing," ACS Sens. **4**, 2746–2753 (2019).

176. J. Zhou, G. Tian, L. Zeng, X. Song, and X. Bian, "Nanoscaled metal-organic frameworks for biosensing, imaging, and cancer therapy," Adv. Healthcare Mater. **7**, 1800022 (2018).

177. S. E. Miller, M. H. Teplensky, P. Z. Moghadam, and D. Fairen-Jimenez, "Metal-organic frameworks as biosensors for luminescence-based detection and imaging," Interface Focus **6**, 20160027 (2016).

178. X. Liu, D. Huang, C. Lai, G. Zeng, L. Qin, H. Wang, H. Yi, B. Li, S. Liu, M. Zhang, R. Deng, Y. Fu, L. Li, W. Xue, and S. Chen, "Recent advances in covalent organic frameworks (COFs) as a smart sensing material," Chem. Soc. Rev. **48**, 5266–5302 (2019).

179. F. Galeotti, M. Pisco, and A. Cusano, "Self-assembly on optical fibers: a powerful nanofabrication tool for next generation 'lab-on-fiber' optrodes," Nanoscale **10**, 22673–22700 (2018).

180. M. Principe, M. Consales, A. Micco, A. Crescitelli, G. Castaldi, E. Esposito, V. La Ferrara, A. Cutolo, V. Galdi, and A. Cusano, "Optical fiber meta-tips," Light Sci. Appl. **6**, e16226 (2017).

181. J. Yang, I. Ghimire, P. C. Wu, S. Gurung, C. Arndt, D. P. Tsai, and H. W. H. Lee, "Photonic crystal fiber metalens," Nanophotonics **8**, 443–449 (2019).

182. S. Kang, H.-E. Joe, J. Kim, Y. Jeong, B.-K. Min, and K. Oh, "Subwavelength plasmonic lens patterned on a composite optical fiber facet for quasi-one-dimensional Bessel beam generation," Appl. Phys. Lett. **98**, 241103 (2011).

183. H. Lin, M.-C. Kao, C.-M. Lai, J.-C. Huang, and W.-C. Kuo, "All fiber optics circular-state swept source polarization-sensitive optical coherence tomography," J. Biomed. Opt. **19**, 021110 (2013).

184. X. Fu, Z. Wang, H. Wang, Y. T. Wang, M. W. Jenkins, and A. M. Rollins, "Fiber-optic catheter-based polarization-sensitive OCT for radio-frequency ablation monitoring," Opt. Lett. **39**, 5066–5069 (2014).

185. G. S. D. Gordon, J. Joseph, T. Sawyer, A. J. Macfaden, C. Williams, T. D. Wilkinson, and S. E. Bohndiek, "Full-field quantitative phase and polarisation-resolved imaging through an optical fibre bundle," Opt. Express **27**, 23929–23947 (2019).

186. K. Schulz, E. Sydekum, R. Krueppel, C. J. Engelbrecht, F. Schlegel, A. Schröter, M. Rudin, and F. Helmchen, "Simultaneous BOLD fMRI and fiber-optic calcium recording in rat neocortex," Nat. Methods **9**, 597–602 (2012).

187. Z. Liang, Y. Ma, G. D. R. Watson, and N. Zhang, "Simultaneous GCaMP6-based fiber photometry and fMRI in rats," J. Neurosci. Methods **289**, 31–38 (2017).